Discovery of persistent quasi-periodic oscillations in accreting white dwarfs: a new link to X-ray binaries

M. Veresvarska [1]⋆ S. Scaringi [1,2] C. Knigge [3] J. Paice [1] D. A. H. Buckley [4,5,6] N. Castro Segura [7] D. de Martino [2] P. J. Groot [4,5,8] A. Ingram [9] Z. A. Irving [3] and P. Szkody [10]

[1]*Department of Physics, Centre for Extragalactic Astronomy, Durham University, South Road, Durham DH1 3LE, UK*
[2]*INAF Osservatorio Astronomico di Capodimonte, Salita Moiariello 16, I-80131 Naples, Italy*
[3]*School of Physics and Astronomy, University of Southampton, Highfield, Southampton SO17 1BJ, UK*
[4]*South African Astronomical Observatory, PO Box 9, Observatory, 7935 Cape Town, South Africa*
[5]*Department of Astronomy, University of Cape Town, Private Bag X3, Rondebosch 7701, South Africa*
[6]*Department of Physics, University of the Free State, PO Box 339, Bloemfontein 9300, South Africa*
[7]*Department of Physics, University of Warwick, Gibbet Hill Road, Coventry CV4 7AL, UK*
[8]*Department of Astrophysics/IMAPP, Radboud University, PO Box 9010, NL-6500 GL Nijmegen, the Netherlands*
[9]*School of Mathematics, Statistics and Physics, Newcastle University, Herschel Building, Newcastle upon Tyne NE1 7RU, UK*
[10]*Department of Astronomy, University of Washington, Seattle, WA 98195, USA*

ABSTRACT

Almost all accreting black hole and neutron star (NS) X-ray binary systems (XRBs) exhibit prominent brightness variations on a few characteristic time-scales and their harmonics. These quasi-periodic oscillations (QPOs) are thought to be associated with the precession of a warped accretion disc, but the physical mechanism that generates the precessing warp remains uncertain. Relativistic frame dragging (Lense–Thirring precession) is one promising candidate, but a misaligned magnetic field is an alternative, especially for NS XRBs. Here, we report the discovery of five accreting white dwarf systems (AWDs) that display strong optical QPOs with characteristic frequencies and harmonic structures that suggest they are the counterpart of the QPOs seen in XRBs. Since AWDs are firmly in the classical (non-relativistic) regime, Lense–Thirring precession cannot account for these QPOs. By contrast, a weak magnetic field associated with the white dwarf can drive disc warping and precession in these systems, similar to what has been proposed for NS XRBs. Our observations confirm that magnetically driven warping is a viable mechanism for generating QPOs in disc-accreting astrophysical systems, certainly in AWDs and possibly also in NS XRBs. Additionally, they establish a new way to estimate magnetic field strengths, even in relatively weak-field systems where other methods are not available.

Key words: accretion, accretion discs – magnetic fields.

1 INTRODUCTION

Accreting white dwarfs (AWDs) are binary systems in which a white dwarf (WD) accretes material from a donor star. The dominant population of AWDs are referred to as cataclysmic variables (CVs) where mass transfer occurs through Roche lobe overflow. In cases where the donor is a degenerate or semidegenerate star they are referred to as AM CVn systems (Solheim 2010).

The WD magnetic field strength can alter the dynamics of the accretion flows in AWDs. If the WD has a sufficiently strong magnetic field ($\gtrsim 10^6$ G) the disc material is disrupted at the magnetospheric radius and is further accreted via the magnetic field lines on to the magnetic poles of the WD. If the magnetic field is strong enough such that the magnetospheric radius lies beyond the disc circularization radius then no disc can form and accretion

proceeds only via accretion streams and columns (both referred to as intermediate polars; Norton, Wynn & Somerscales 2004; Norton et al. 2008). For systems possessing the strongest WD magnetic fields, the accretion flow only follows the magnetic field lines and the WD spin and system orbital period are synchronized (systems referred to as polars; Cropper 1990).

Quasi-period oscillations (QPOs) are non-coherent brightness variations in the X-ray flux, widely recognized in X-ray binary systems (XRBs). In the context of XRBs, the flux fluctuations manifest as characteristically broad features in the power spectra, due to the unstable quasi-periodic nature of the signal. They are present both in neutron star (NS) and black hole (BH) XRBs with a variety of different types (see Ingram & Motta 2019 for a detailed review). BH XRBs exhibit low ($\lesssim 30$ Hz) and high ($\gtrsim 60$ Hz) frequency QPOs, with low-frequency QPOs being somewhat more common. The low-frequency QPOs show different broad types, depending on their strength, width and frequency, one of which is known as Type-C. The broadness of a QPO is characterized by its quality factor $Q = \frac{\nu_0}{2\Delta}$,

where ν_0 is the centroid frequency of the Lorentzian representing the QPO and Δ its half-width at half-maximum (HWHM). Type-C QPOs in particular are strong and narrow, with $Q \gtrsim 8$, and are also known to display strong harmonics. Similarly, NS XRBs show kHz QPOs and low-frequency QPOs, however as opposed to BH XRBs the kHz QPOs are more common. They also display colour evolution on the hardness–intensity diagram, similarly to BH XRBs (Homan 2001; Belloni & Motta 2016). Based on the QPO–colour evolution they are classified as flaring branch oscillations (FBO), normal branch oscillations (NBO) and horizontal branch oscillations (HBO). Type-C and HBO QPOs are known to follow a linear correlation with a broad-band aperiodic low-frequency break (Wijnands & van der Klis 1999), with a characteristic decrease in power with increasing frequency.

There have been numerous QPOs reported in AWD systems in the literature (see e.g. Warner 2004 for review). The QPOs in the context of AWDs, as opposed to XRBs, usually refer to a transitional and temporary periodic signal in the optical whose amplitude can vary significantly. The first report of a QPO in AWDs was in Patterson, Robinson & Nather (1977), where a fast ($\sim$50s) oscillation in the light curve was detected in the outburst of RU Peg. Another type of quasi-periodic signals in AWDs are so-called dwarf novae oscillations (DNOs) (Warner & Robinson 1972), which, however, appear to display a somewhat more coherent period. One possible explanation is that these are associated to g-mode pulsations of the WD (Warner & van Zyl 1998; Townsley & Bildsten 2004; Woudt et al. 2005; Townsley, Arras & Bildsten 2016). The DNO periods are usually quite fast ($\sim$10 s) and follow a relation to the longer QPOs so that $P_{QPO} \approx 16 \times P_{DNO}$. In Warner, Woudt & Pretorius (2003) a further sub-type of DNOs ($P_{DNO} \sim$20s), the long-period DNOs (lpDNOs with $P_{lpDNO} \sim 80-100$ s) are also discussed. These are thought to be empirically related to the DNOs and QPOs such that $P_{lpDNO} \approx P_{DNO} \approx \frac{1}{4} P_{QPO}$ and are usually associated to high mass transfer rate systems and are sometimes detected as doubles.

Other types of QPOs in AWDs have been observed, such as the broad feature in the high state of magnetic AWD TX Col (Littlefield et al. 2021). The QPO in TX Col as observed by *TESS* spans from $\sim$10 to $\sim$20 d^{-1} and in width resembles the QPO in AM CVn SDSS J1908+3940 reported by Kupfer et al. (2015). These broad QPOs and their lack of harmonics resembles more a broad-band feature of the power spectral distribution (PSD) most likely associated to mass transfer variation in the accretion disc (see Scaringi 2014), rather then a quasi-coherent signal as in XRBs. Similarly to Warner et al. (2003), all of these QPOs have been detected in the optical, with no known X-ray counterparts. The study by Warner et al. (2003) extensively reports QPOs in AWD systems, drawing a comparison between the reported QPOs to those observed in XRBs (Wijnands & van der Klis 1999). WZ Sge, a target in Warner et al. (2003) and also studied in this work, was reported to exhibit short-period DNOs at $\sim$27.87 and 28.95 s and an $\sim$740 s QPO. While the 27.87 s signal has been linked to the spin of WZ Sge (Patterson 1980), the QPO is attributed to the retrograde precession of a geometrically thick disc (Warner & Woudt 2002). However, the absence of an $\sim$740 s QPO signal in WZ Sge from *TESS* short cadence data and other objects displaying QPOs in Warner et al. (2003) suggests these signals are transitional. It is also important to note that the reported correlation between AWDs and XRBs in Warner et al. (2003) is not based on broad-band features and QPO frequencies, but rather on transitional QPOs and DNOs, which may represent a separate class of signals. Therefore, the presence of these signals in AWDs could be driven by a different physical process than those observed in XRBs. A further important distinction between all of the above-reported QPOs in

AWDs and XRBs is, that there have never been reported harmonics of any kind of QPOs in AWDs, as opposed to XRBs.

Here, we try to characterize QPOs in AWDs in direct analogy to those in XRBs using self-similar analysis techniques in order to better understand their physical origin. In doing so, we report the discovery of five AWD systems showing persistent QPOs in optical detected by *TESS* at ~ 1.3–3×10^{-4} Hz (1–2 h), which we use to revise the relation to XRBs. We also report on the first instance of harmonics being discovered for QPOs in AWDs in three of the five reported systems. *TESS* has an archival database of $\sim$1200 AWDs, with even more AWD candidates. After visually inspecting the closest sample of AWDs we recovered the five examples reported here. However, it is likely that many more are present in the TESS database and that many more could be uncovered with an instrument with a better signal-to-noise ratio. In Section 2, the observations used are described. Section 3 discusses the methods and analysis used as well as the construction of the time-averaged power spectra (TPS) with a similar methodology to what is conventionally employed in analysis of QPOs in XRBs (Sections 3.1 and 3.2). We also discuss the statistical significance of the observed broad-band frequency features in the PSD used in the analysis (Section 3.3). In Section 4, we report that the QPOs and broad-band components of the TPS fit from Section 3.2 appear to follow the observational correlation between the QPO frequency and the low-frequency break from Wijnands & van der Klis (1999). In Section 5, we introduce a proposed model to explain the observed QPOs, based on magnetically driven precession of the inner accretion flow due to the interaction between a weak accretor magnetic field and its inner accretion flow. We then discuss the implications of the aforementioned results with conclusions drawn in Section 6.

2 OBSERVATIONS

The data used in this work were obtained by *TESS* and can be accessed on the Mikulski Archive for Space Telescopes (MAST[1]). *TESS* is a space-based mission that observes the entire sky with four cameras and a 24×96 deg^2 continuous field of view. For a selected number of targets, it produces photometry with either 2 min or 20 s cadence and an overall full frame image of the CCD is available each 30 or 10 min. A detailed description of the instrument can be found in the *TESS* Instrument Handbook.[2] The observing strategies of *TESS* split the sky into southern and northern sectors, each 24×96 deg^2 in size and observes each sector for 1 month. Including the downlink time and other technical procedures this translates to ~ 27 d worth of scientific data for each sector.

The details of the number of *TESS* sectors available for each object studied here, as well as the chosen cadence, are presented in Table 1. The short cadence was used for the objects that had all the available sectors in 20 s cadence (WZ She and GW Lib). If the short 20 s cadence was only available for some of the sectors, 120 s cadence was used for those particular objects (CP Pup, T Pyx, and V3101 Cyg).

TESS data were downloaded and cosmic rays were removed using the LIGHTKURVE package.[3] The simple aperture photometry (SAP) flux is used to retain intrinsic variability of the systems while avoiding

Table 1. Summary of the *TESS* data of WZ Sge, CP Pup, GW Lib, T Pyx, and V3101 Cyg with sector numbers and dates. The used exposure time of *TESS* sectors is noted for each sector, keeping it constant for each object. The optimal segment length p_0 used for constructing TPSs in 3.1 is noted as well as whether the *TESS* data is converted into flux in mJy or kept in *TESS* default $e^-\,s^{-1}$.

Name	TIC	Sector	Dates	t_{exp} (s)	p_0 (d)	Calibration
WZ Sge	86408822	41	20/07/21–20/08/21	20	6	–
		54	09/07/22–05/08/22	20	6	–
CP Pup	14560527	7	08/01/19–01/02/19	120	10	*ASAS-SN*
		8	02/02/19–27/02/19	120	10	*ASAS-SN*
		34	14/01/21–08/02/21	120	10	*ASAS-SN*
		35	09/02/21–06/03/21	120	10	*ASAS-SN*
		61	18/01/23–12/02/23	120	10	*ASAS-SN*
GW Lib	225798235	38	29/04/21–26/05/21	20	10	–
T Pyx	17897279	35	09/02/21–06/03/21	120	7	–
		62	12/02/23–10/03/23	120	7	–
V3101 Cyg	1974089138	55	05/08/22–01/09/22	120	10	–

the transit detection optimization of the pre-search data conditioning flux. Data points are further excluded if their quality flag > 0.

TESS provides photometry in units of $e^-\,s^{-1}$, which does not provide any information on the absolute flux of the target, only relative brightness. To obtain absolute photometry in mJy, we attempt to convert these measurements using quasi-simultaneous ground-based observations from *ASAS-SN*, without accounting for any bolometric correction. This conversion is based on assuming a linear relation between the *TESS* and *ASAS-SN* fluxes. This method has been previously used (Scaringi et al. 2022; Veresvarska et al. 2024), but it requires quasi-simultaneous coverage of the target by both *TESS* and *ASAS-SN*. Such coverage was achieved only for CP Pup, as detailed in Veresvarska et al. (2024). For the remaining targets, no conversion is adopted, due to lack of quasi-simultaneous coverage by *TESS* and *ASAS-SN*, whereas this does not pose a problem for the analysis presented in this paper, lack of ground-based calibration prohibits any measurements of the energetics being made. We note that with the advent of more synoptic sky surveys (e.g. BlackGEM Groot, Bloemen & Vreeswijk 2024) space-based calibrations will be more easily achieved due to wider sky coverage.

There is a linear trend in the data of GW Lib and V3101 Cyg, which has been removed using a similar methodology as in Kupfer et al. (2015). Similar linear trends due to systematic effects have often been found to affect long-term data, especially in the *Kepler* and *K2* missions (Kupfer et al. 2015; Solanki et al. 2021). These trends can alter the flux levels over time and induce low-frequency power excess and hence need to be removed. This is done by fitting a linear trend to the light curve smoothed on a 2 h time-scale which is subsequently subtracted from the original light curve. The correction was done for the whole sector for GW Lib and for each half sector for V3101 Cyg by fitting a straight line to the time-averaged light curve and correcting the non-averaged light curve for the obtained trend. The corrected light curve of CP Pup has already been reported in Veresvarska et al. (2024), while the remaining targets are shown in Fig. A1. WZ Sge shows a greater amplitude of variability akin to an envelope in sector 54. This is also seen in CP Pup (Bruch 2022; Veresvarska et al. 2024) and is thought to be an instrumental effect as it is displayed in multiple objects in the same sector, e.g. TIC 1909750039, TIC 1688054795, and TIC 1713691071 in sector 54 all show a similar envelope. This is not corrected for, but the analysis as described in Section 3 has been conducted on sectors 41 and 54 separately. Since it has been found that the results are robust to any changes between the two sectors, it is assumed that the effect of the envelope on the results is negligible.

For targets with more than one sector (WZ Sge and T Pyx), the combination of the different sectors using uncalibrated *TESS* absolute photometry is possible because the combination happens in frequency domain, where separate power spectra are combined after they have been rms normalized. In such a case, the relative variability in separate sectors is conserved and does not affect the overall result. As a test, we have conducted the same analysis on un-calibrated *TESS* data of CP Pup and found no significant differences.

3 METHODS AND ANALYSIS

To draw an analogy to XRBs and the QPOs they exhibit, we attempt to reproduce their analysis as closely as possible. This involves construction of a TPS (as described in detail in Section 3.1 and shown in Fig. 1) instead of inspecting a non-averaged and non-binned PSD (Fig. B1). The details of the broad-band PSD fits are described in Section 3.2, where the broad-band components of the TPS are fitted with zero-centred Lorentzians akin to XRBs. Section 3.3 discusses the significance of the lowest frequency broad-band component of the fit from Section 3.2.

3.1 Broad-band structure of the time-averaged power spectrum

We here characterize the broad-band variability and QPOs using TPS as is conventionally done when studying XRBs (Belloni, Psaltis & van der Klis 2002; Ingram & Motta 2019). TPS are usually constructed by separating the light curve into non-overlapping segments of equal length and computing the Fourier transform for each segment. The resulting power spectra are then averaged and re-binned on to a coarser frequency grid to reduce uncertainty. The error on the normalized power in each frequency bin corresponds to the standard error on the mean. In XRBs, the nature of X-ray timing requires the use of fast Fourier transform. Here, we adopt the Lomb–Scargle (Lomb 1976; Scargle 1998) algorithm as the data obtained from *TESS* is not strictly evenly sampled due to gaps in the data from data downlinks and exclusion of some data points due to instrumental effects or other anomalous events. The Lomb–Scargle implementation used is ASTROPY v.5.3.4 with the limiting upper frequency set to the Nyquist frequency based on the sampling in Table 1 and the lower frequency set to $3 \times (L)^{-1}$, where L is the length of the light curve. The oversampling factor is set to 1. The resulting power spectrum is normalized so that the total power of the power spectrum corresponds to $\frac{\sigma}{\text{rms}^2}$, where σ is the variance of
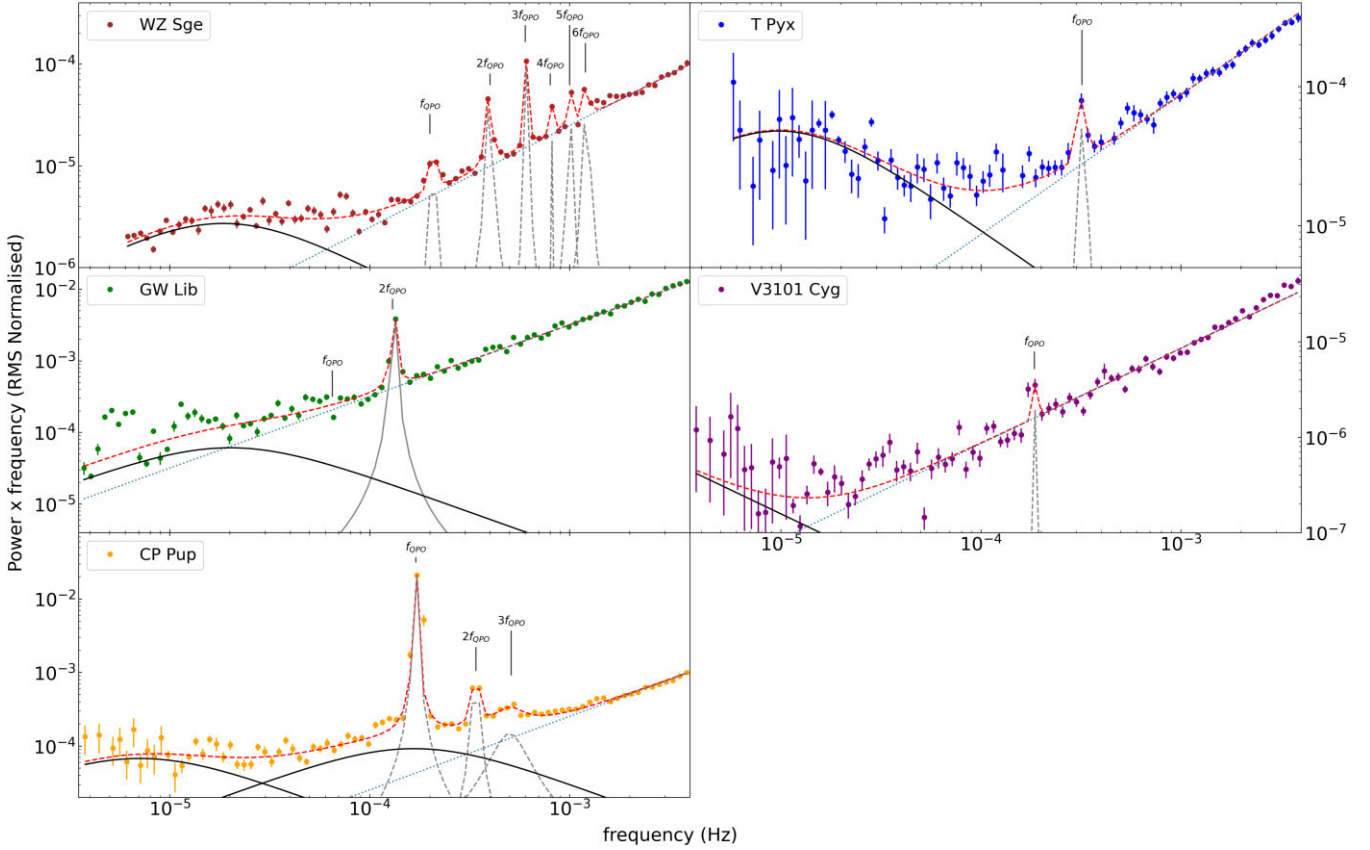
Figure 1. TPS of WZ Sge, GW Lib, T Pyx, V3101 Cyg, and CP Pup averaged on the segment lengths specified in Table 1 with 90 logarithmicaly spaced bins. The empirical fit of the PSD is included here and comprises a Poisson noise power law (dotted line) in the high frequencies, one (in the case of WZ Sge, GW Lib, T Pyx and V3101 Cyg) or two (CP Pup) zero-centred Lorentzians (solid line) representing the broad-band PSD structure and Lorentzians representing the QPOs and their harmonics (dashed line).

the light curve and rms is the root mean square. The resulting TPSs of WZ Sge, CP Pup, GW Lib, T Pyx, and V3101 Cyg are shown in Fig. 1.

In Fig. 1, the segment length that is used to construct the TPSs is specified for each object in Table 1. After testing the robustness of the fit in Section 3.2 by varying the segment length, the length with the best visualization of the PSD features was chosen. A similar method was used to select the number of frequency bins ($N_{bins} = 90$), ensuring that the frequency resolution remains high enough to clearly distinguish QPOs from the broad-band PSD structure. This results in a rebinning factor of 270 for WZ Sge, 45 for T Pyx, 468 for GW Lib, 80 for V3101 Cyg, and CP Pup.

The TPSs are also cleaned of the orbital signal, where present. This is not necessary for XRBs as most XRBs have orbital signals of the order of several hours, where the signal does not interfere with QPOs present on time-scales of ~seconds. The power originating from the orbital motion is removed after computing the Lomb–Scargle for each segment. For each segment, the peak of the orbital period is identified and ~25 points on each side of the peak are removed, varying the number as necessary according to the strength and width of the signal. The same process is then repeated for 10 following harmonics of the orbit, 20 in the case of WZ Sge. The number of removed points was chosen after visual inspection to confirm that this would not remove any variability intrinsic to the QPO or significantly affect the broad-band PSD. This process is chosen over pre-whitening the light curve to avoid any possible changes to the

underlying broad-band variability. Fig. 1 displays the TPSs with the orbital variability already removed for WZ Sge, T Pyx, and V3101 Cyg. The linear PSD with the orbital periods included can be seen in Fig. B1. The process was not necessary for GW Lib due to the low inclination of the system causing the orbital period to be only detectable spectroscopically (Thorstensen et al. 2002). Due to the lack of any periodic signals in the power spectrum of CP Pup and the uncertain nature of its orbital period (Veresvarska et al. 2024), no orbital period variations were removed.

3.2 Time-averaged power spectra

The broad-band structure of systems that accrete via an accretion disc can usually be fitted well with a sum of Lorentzian components (Belloni et al. 2002):

$$P_{L}(\nu) = \frac{r^2 \Delta}{\pi} \frac{1}{\Delta^2 + (\nu - \nu_0)^2}, \tag{1}$$

where $P_{L}(\nu)$ is the RMS normalized power, Δ is the HWHM and r is a normalization factor proportional to the integrated fractional rms. ν_0 represents the centroid frequency, which is set to 0 in the case of zero-centred Lorentzians. In the case of non-zero centred Lorentzians, where $\nu_0 > 0$, the frequency of the peak of the PSD feature is given by

$$\nu_{max} = \sqrt{\nu_0^2 + \Delta^2}. \tag{2}$$

Therefore, the PSDs in Fig. 1 are fitted with a number of non-zero centred Lorentzians corresponding to the number of quasi-periodic signals and their harmonics, plus one or two zero-centred Lorentzians representing the broad-band structure of the PSD. Two zero-centred Lorentzians were necessary only in the case of CP Pup. This is most likely due to the Poisson noise (see below) contributing mostly at high frequencies and intrinsic broad-band variability becoming dominant at $\sim 10^{-3}$ Hz. This can be seen in Fig. 1 at the frequency where the Poisson noise component overtakes the zero-centred Lorentzian broad-band component. By contrast, this changeover occurs at $\sim 10^{-4}$ Hz for WZ Sge, GW Lib and V3101 Cyg.

The Poisson noise is another component of the PSD that needs to be considered. It can be represented by a constant, so that $P(\nu) = A$, where A represents the amplitude of the noise.

The PSD is fitted with all the free parameters for each object listed in Table 2. The overall PSD model is hence expressed as

$$P_\nu = \sum_{i=0}^{N_{\mathrm{QPO}}} P_{\mathrm{L}}\left(r_i, \Delta_i, \nu_{0,i}, \nu\right) + \sum_{j=0}^{N_{\mathrm{L_0}}} P_{\mathrm{L_0}}\left(r_j, \Delta_j, \nu\right) + A. \qquad (3)$$

Here, P_{L} is a non-zero-centred Lorentzian representing the quasi-periodic signals and their harmonics, $P_{\mathrm{L_0}}$ corresponds to the zero-centred Lorentzians, and A accounts for the Poisson noise.

The best-fitting parameters with the corresponding errors are shown in Table 2. The best fit is determined using the Levenberg–Marquardt least-squares fitting method with keeping all parameters free. Given the number of free parameters in the fit (e.g. 21 for WZ Sge) it is not feasible to conduct a full parameter sweep to determine the true confidence contours. Instead an assumption that the correlation between individual parameters is not dominant is made. In such a case, a rough estimate of errors can be made by fixing all parameters to the best-fitting value and varying a single parameter to determine the one-dimensional confidence contours of 99.7 per cent. This technique was adapted from QPO fitting procedures in XRBs in cases where no strong correlations between PSD components can be assumed. This is applicable here due to the narrowness of the QPOs and the low number of zero-centred Lorentzians required to fit the individual PSDs. Further complications may, however, arise from the unevenly spaced data causing the frequency bins to not be strictly independent. Despite this, it is important to note that the method cannot provide the exact 99.7 per cent confidence contours, but can serve as a lower limit.

3.3 Break significance

The uncertainty on the low-frequency broad-band feature (break) measured in Table 2 is difficult to constrain due to several factors. One relates to the logarithmic spacing of the frequency bins resulting in a decrease of the number of points in the lower frequency bins, increasing their error. Therefore, it is necessary to verify the presence of any break as opposed to a red noise-related power law.

To generate light curves that follow a specific power-law pattern, we use an algorithm similar to the one described by Veresvarska & Scaringi (2023), based on the method developed by Timmer & König (1995). Given a PSD model, the algorithm will generate a simulated PSD by scattering the amplitudes and phases around the PSD model. The randomized PSD is then transformed back into the time domain using an inverse Fourier transform, creating a light curve with the desired PSD shape.

In this case, the PSD shape is almost the same as the one outlined in Table 2. However, the lowest frequency zero-centred Lorentzian is replaced by a power-law fit, as shown in Fig. 3, where the power law

is defined by $P_{\mathrm{power\,law}} = A\nu^\alpha$. The Lorentzians corresponding to the QPOs are removed, and the other parameters from Table 2 are kept constant. The values for A and α are found using the Levenberg–Marquardt least-square method. The reduced χ^2_ν for the fits are also noted in Table 3. It is worth noting that all objects apart from V3101 Cyg have a significantly higher χ^2_ν for the power-law fit than when the zero-centred Lorentzians are used.

The parameters from Table 2, combined with the best-fitting values of A and α, are used to generate artificial light curves. The components involved in this process are listed in Table 3. In this context, r_{last} and Δ_{last} refer to the parameters of the lowest frequency zero-centred Lorentzian for a given object in Table 2. The errors shown in Table 3 are calculated in the same way as those in Table 2, as detailed in Section 3.2.

The process of generating artificial light curves is repeated 1000 times, resampling the final output on the time stamps of the original *TESS* light curves, reproducing identical PSDs as in Fig. 1. All the points in each frequency bin are examined and fitted with a χ^2 distribution. The optimal fit of the χ^2 distribution is obtained again with the Levenberg–Marquardt least-square method. The 3σ and 5σ confidence contours corresponding to 93.32 and 99.977 per cent levels are extracted and shown in Fig. 2. The envelopes determine the significance level of RMS in each frequency bin independently. Therefore, any observed trend in deviation from a certainty envelope signifies a higher level of confidence that the input power law does not represent a viable model for the PSD.

The resulting certainty envelopes are shown for all objects in Fig. 2. It is clear that WZ Sge contains a feature, that cannot be explained by a simple power law, with a certainty over 5σ. Other deviations from the certainty envelope such as the QPO with its harmonics shows the significance of the QPO signal. Other such features similar to the bump at $7-8 \times 10^{-5}$ Hz represent broad-band features that were not included in the PSD fit. Similar deviations at frequencies $> 10^{-3}$ Hz are influenced by the remaining harmonics of the QPO that were not fitted as their corresponding frequency bins did not allow for separation of individual harmonics.

No significant deviation from the 5σ significance envelope is seen in any other objects apart from WZ Sge. The long-term TPS of AWDs are known to have a complex structure requiring multiple Lorentzians (Scaringi et al. 2012). However, using the 3σ and 5σ confidence contours it is difficult to say to what extent this structure translates to the objects here, apart from the clear example of WZ Sge. Some structure is hinted at in GW Lib, but it is obstructed by the dominant Poisson noise component and limited amount of data available (compared to WZ Sge and MV Lyr in Scaringi et al. 2012).

Despite not being able to probe low enough frequencies to test the presence of a low-frequency break with $\gtrsim 5\sigma$ significance in all the systems, the obtained significance combined with the χ^2 comparison of the two fits, shows evidence of self-similar empirical features to those in broad-band PSDs in XRBs. A zero-centred Lorentzian is used across all five systems, since the majority of the targets show a significantly lower χ^2 for the zero-centred Lorentzian fit. However, to err on the cautious side, the uncertainties on the break component are treated as an upper limit in all targets apart from WZ Sge.

4 RESULTS

In this section, the main results are outlined. The new QPOs in AWDs are reported in terms of the existing QPOs and broad-band low-frequency break correlation from Wijnands & van der Klis (1999). The link to QPOs in XRBs is drawn from the broadness of the signal in the power spectrum as seen in Fig. B1 and explained further in

Table 2. Results of the empirical fit to the PSDs from Fig. 1.

	WZ Sge	CP Pup	GW Lib	T Pyx (s)	V3101 Cyg
$A\ (\times 10^{-2})$	$2.5^{+0.2}_{-0.2}$	25^{+2}_{-2}	56^{+5}_{-5}	$8.5^{+0.8}_{-0.8}$	$8.7^{+0.8}_{-0.8} \times 10^{-2}$
$r_1 (\times 10^{-2})$	$1.0^{+0.3}_{-0.4}$	59^{+10}_{-10}	6^{+4}_{-6}	7^{+3}_{-7}	$1.1^{+0.8}_{-1.1} \times 10^{-1}$
$\Delta_1 (\times 10^{-8})$	4^{+3}_{-3}	70^{+30}_{-30}	2^{+4}_{-2}	$0.7^{+0.9}_{-0.7}$	$0.1^{+0.2}_{-0.1}$
$\nu_{0,1} (\times 10^{-4})$	$2.07^{+0.05}_{-0.04}$	$1.70^{+0.1}_{-0.05}$	$1.33^{+0.01}_{-0.05}$	3^{+2}_{-2}	$1.8665^{+1}_{-0.0009}$
Q_1	~ 2600	~ 120	~ 3300	$\sim 21\,000$	$\sim 93\,000$
$r_2 (\times 10^{-2})$	$0.21^{+0.05}_{-0.06}$	10^{+2}_{-2}	$1.0^{+0.3}_{-0.4}$	$1.7^{+0.2}_{-0.2}$	$1.9^{+0.8}_{-1.5}$
$\Delta_2 (\times 10^{-5})$	$0.7^{+0.7}_{-0.4}$	$7^{+4}_{-4} \times 10^{-3}$	$1.6^{+2.8a}_{-1.2}$	$1.0^{+0.3a}_{-0.5}$	$0.13^{+0.13a}_{-0.13}$
$\nu_{0,2} (\times 10^{-4})$	$4.0^{+0.1}_{-0.1}$	$3.4^{+0.1}_{-0.1}$	–	–	–
Q_2	~ 30	~ 2500	–	–	–
$r_3 (\times 10^{-2})$	$1.1^{+0.3}_{-0.4}$	$1.0^{+0.2}_{-0.3}$	–	–	–
$\Delta_3 (\times 10^{-4})$	$1.4^{+0.7}_{-0.7} \times 10^{-3}$	$1.0^{+2}_{-0.5}$	–	–	–
$\nu_{0,3} (\times 10^{-4})$	$6.1^{+0.2}_{-0.2}$	$4.9^{+0.6}_{-0.7}$	–	–	–
Q_3	~ 2200	~ 2.5	–	–	–
$r_4 (\times 10^{-2})$	13^{4}_{-6}	$2.4^{+0.2}_{-0.3}$	–	–	–
$\Delta_4 (\times 10^{-4})$	$1.5^{+1}_{-1} \times 10^{-5}$	1.7^{+8}_{-5}	–	–	–
$\nu_{0,4} (\times 10^{-4})$	8^{+4}_{-7}	–	–	–	–
Q_4	~ 2.7	–	–	–	–
$r_5 (\times 10^{-2})$	$1.7^{+0.5}_{-0.8}$	$2.1^{+0.4}_{-0.4}$	–	–	–
$\Delta_5 (\times 10^{-7})$	$1.0^{+0.7}_{-0.7}$	70^{+50a}_{-30}	–	–	–
$\nu_{0,5} (\times 10^{-4})$	$1.0^{+0.2}_{-0.2}$	–	–	–	–
Q_5	~ 500	–	–	–	–
$r_6 (\times 10^{-2})$	$1.6^{+0.5}_{-0.7}$	–	–	–	–
$\Delta_6 (\times 10^{-7})$	3^{+2}_{-2}	–	–	–	–
$\nu_{0,6} (\times 10^{-3})$	$1.22^{+0.03}_{-0.02}$	–	–	–	–
Q_6	~ 200	–	–	–	–
$r_7 (\times 10^{-3})$	$4.1^{+0.3}_{-0.3}$	–	–	–	–
$\Delta_7 (\times 10^{-5})$	$1.9^{+0.4a}_{-0.3}$	–	–	–	–
χ^2_ν	6.16	3.41	1.95	1.52	5.26

[a]The lowest frequency zero-centred Lorentzian used in Figs 4 and 7. *Notes.* The independent columns correspond to different objects and the rows correspond to model components: A – Poisson noise amplitude, r_i – integrated fractional rms of a given Lorentzian, Δ_i – half-width half-maximum of a given Lorentzian, $\nu_{0,i}$ – centroid frequency of a given Lorentzian (only Lorentzians representing QPOs and their harmonics have this component). The Q value for each Lorentzian representing a QPO is given as well and is denoted by Q_i. Broad-band component Lorentzians are zero-centred and their $\nu_0 = 0$ by default and is not denoted here.

**Table 3.** Results of the empirical fit to the PSDs from Fig. 2.

	WZ Sge	CP Pup	GW Lib	T Pyx (s)	V3101 Cyg
A	$9^{+2}_{-2} \times 10^{-10}$	$2^{+8}_{-2} \times 10^{-8}$	$1 \times 10^{-4+4}_{-1\times 10^{-4}}$	$5^{+2}_{-2} \times 10^{-9}$	$1^{+13}_{-1} \times 10^{-13}$
α	$-1.756^{+0.003}_{-0.004}$	$-1.684^{+0.005}_{-0.004}$	$-0.883^{+0.004}_{-0.003}$	$-1.778^{+0.004}_{-0.005}$	$-2.248^{+0.010}_{-0.009}$
χ^2_ν	163	11.6	14.5	5.2	5.00

Notes. The independent columns correspond to different objects and the lines correspond to model components: A – power-law amplitude and α – power-law index.

Section 5.1. Another important characteristic of the new QPOs in AWDs is that it is the first instance in which QPOs in AWDs are reported to show harmonics as seen in Fig. 1.

As mentioned before in Section 1, type-C and HBO QPOs in XRBs show a linear correlation with a low-frequency break in their PSDs. The break corresponds to the nearest low zero-centred Lorentzian that is used in the fit of the broad-band PSD and was first reported in Wijnands & van der Klis (1999) with an overview available in Ingram & Motta (2019).

The results of taking the lowest zero-centred Lorentzian component from Table 2 (denoted by [a]) and plotting it against the characteristic QPO frequency as defined in equation (2) is shown in Fig. 4. Since for GW Lib the fundamental of the QPO signal reported by Chote et al. (2021) is not detected in *TESS*, half of the second harmonic frequency (Δ_1 and $\nu_{0,1}$ from Table 2) is used instead. Following from Section 3.3 only upper limits are used for the zero-centred Lorentzian in all systems apart from WZ Sge and are denoted by arrows. BH and NS QPOs with their corresponding low-frequency
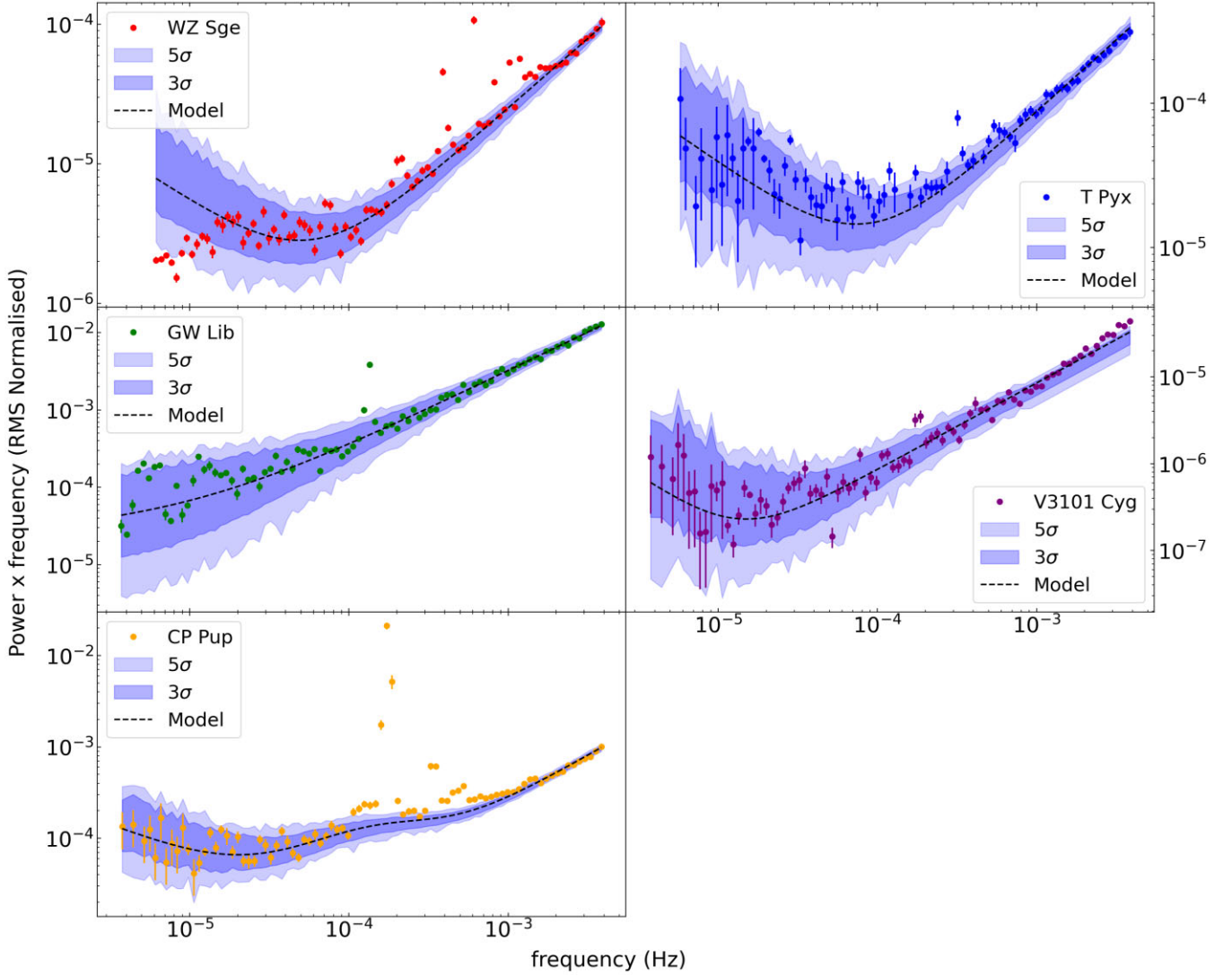
Figure 2. PSDs as shown in Fig. 1. Shaded regions show confidence contours from Timmer & König (1995) algorithm. Dark-shaded region corresponds to 3σ significance and light-shaded region to 5σ significance. The data points outside of the shaded regions boundaries denote that the input power law (dashed line) cannot explain the underlying PSD shape to 3σ or 5σ significance. The QPOs are outside of the 3σ and 5σ significance since their respective Lorentzians have not been included in the model. This showcases their $>> 5\sigma$ significance above the underlying power law.

broad-band components (breaks) from table 1 in Wijnands & van der Klis (1999) are also shown.

The points representing AWDs are clearly following the same empirical relation as the XRBs from Wijnands & van der Klis (1999). The AWDs are several orders of magnitude lower in both QPO and break frequency. To demonstrate the significance of this correlation a linear fit is obtained using linear least-squares regression as implemented in SCIPY. A Pearson correlation coefficient of 0.991 is obtained for all data shown in Fig. 4 and 0.805 for XRBs only. The resulting linear trend is shown in Fig. 4 as a solid line for all data and as a dashed line for solely XRBs. Bootstrapping is used to test the robustness of this correlation. This consists of randomizing the QPO frequencies for corresponding break frequency values. In doing so, no correlation is expected and the Pearson correlation coefficient is expected to be ~0. Repeating this process 10^4 times then shows that the correlation is significant to 99.99 per cent confidence. The resulting distribution of the Pearson correlation coefficient is then shown in the bottom panel of Fig. 3. To constrain the uncertainty

on these fits, N data points are randomly selected with replacement from the data set in Fig. 4. The linear regression fit is then repeated and the Pearson coefficient is computed. The process is repeated 10^4 times resulting in the mean Pearson coefficient of 0.991±0.005, a value consistent with the original Pearson correlation coefficient. This process is repeated for all data points in Fig. 4 as well as only XRB points with the resulting distributions shown in Fig. 3. The uncertainty in the linear regression fits performed during bootstrapping is shown in Fig. 4 as the lightly shaded regions for all data points and for XRBs only. The correlation can hence be expressed as $\log(\nu_{QPO}) = 0.87 \pm 0.03\log(\nu_{break}) + 0.72 \pm 0.05$ for all data points and $\log(\nu_{QPO}) = 0.86 \pm 0.06\log(\nu_{break}) + 0.73 \pm 0.05$ for XRBs only.

5 DISCUSSION

In this section, the implications of the QPO model as a potential tool for spin period and magnetic field strength measurement for weakly
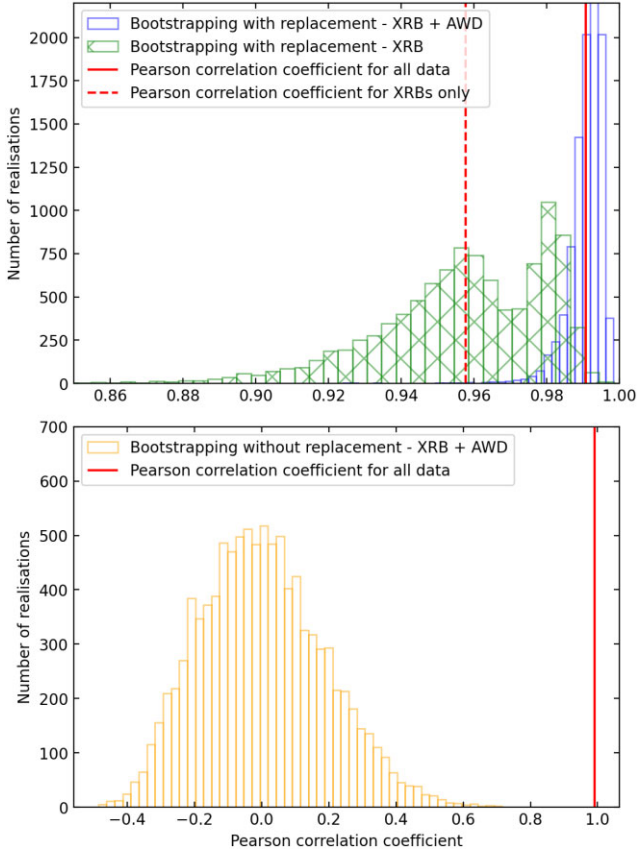
Figure 3. Top panel: distribution of the Pearson correlation coefficient for the bootstrapping of data from Fig. 4 with replacement. The clear distribution corresponds to bootstrapping of all data, whilst the hatched distribution only drew from the XRB sample from Fig. 4. The solid line represents the Pearson correlation coefficient of all data in Fig. 4 and the dashed line corresponds to the value of the coefficient when AWDs are excluded. Bottom panel: the distribution of the Pearson correlation coefficient resulting from bootstrapping the data from Fig. 4 without replacement and by randomizing one of the axes. The zero-centred distribution shows the 99.99 per cent significance of the correlation from Fig. 4, with the solid line marking the value of the Pearson correlation coefficient of the data.

magnetized AWDs is discussed in Section 5.2. In Section 5.3, the QPO and break correlation for XRBs is discussed in the framework of AWDs and the implications for the driving mechanisms of the QPOs.

5.1 Possible interpretations of QPOs in AWDs

There are numerous signals which are present in AWDs in the frequency range displaying the QPO signals shown in Fig. 1.

The PSDs in Fig. 1 are already cleaned of any variability related to the orbital period of the systems. Inspecting the nature of the signals in the non-averaged and non-binned power spectra in Fig. B1, we find that the signals are phenomenologically different from the coherent signals usually present in AWDs, such as the orbital period or spin. The main difference being the power peaks of the signals are broader than coherent periods. Where present, the signal from the orbital period is also indicated in Fig. B1.

Another type of coherent signal present in AWDs is usually due to negative and positive superhumps and their associated fundamental signals. In that case, the superhumps are present relatively close to the orbital period of the system. For a positive superhump, $\nu_{SH}^+ <$
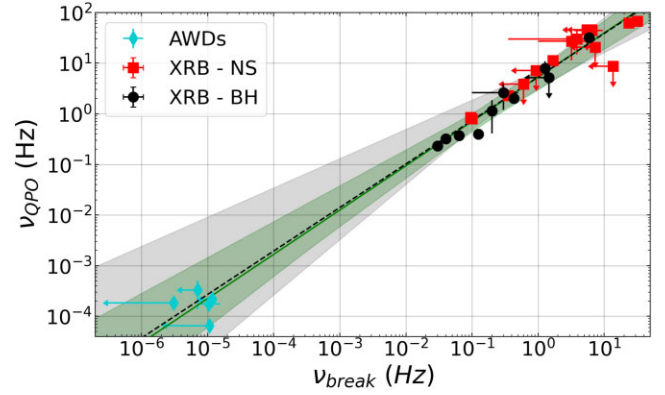
Figure 4. QPO frequency as a function of the break frequency. The observed QPOs with their corresponding low-frequency breaks are denoted for AWDs in diamonds, for NS XRBs in squares and in filled circles for BH XRBs. For AWDs, these are taken from the empirical fit in Section 3.2 and Table 2. The QPO frequency is the peak frequency as denoted in equation (2) using Δ_1 and $\nu_{0,1}$. The only exception is GW Lib where the QPO frequency is taken as half that, since only the first harmonic of the QPO is detected in *TESS* with its true fundamental being reported in Chote et al. (2021). The break frequencies are denoted in Table 2 by [a] for each object. The solid line represents the fit to the data from linear least-squares regression and the shaded darker area represents the uncertainty on the fit. The dashed line represents the fit to the data when AWDs are excluded, with the uncertainty being represented by the lighter shaded region.

ν_{orb}, and the signal is associated with the tidal stresses exerted by the secondary on the disc. These cause the disc to become eccentric and undergo apsidal precession in the prograde direction (Lubow 1991). In this scenario, only GW Lib and V3101 Cyg would qualify. In neither system is a fundamental frequency of the signal found at low frequencies. For the case of negative superhumps, where $\nu_{SH}^- > \nu_{orb}$, the signal is thought to be caused by the retrograde nodal precession of a tilted accretion disc (Wood, Thomas & Simpson 2009), resulting in a 3:1 resonance. This is viable for WZ Sge and T Pyx. However, in the case of WZ Sge, CP Pup, GW Lib, and T Pyx, the QPO signal shows distinct harmonics, making a superhump explanation unfeasable. The presence of harmonics also rules out any other possibility of the signals being related to a beat between the orbit and spin.

Another peculiar feature of the signals is that they are not entirely coherent, as shown in Fig. B1. As opposed to the orbital signals, the QPO signals are broad, reaching a width of $\sim 2 \times 10^{-5}$ Hz. They also exhibit slight variations in central frequency, amplitude, and shape. This has already been reported for CP Pup (Bruch 2022; Veresvarska et al. 2024). In GW Lib, the signal is revealed to be the first harmonic of the fundamental signal at ~ 4 h, interpreted as a quiescent superhump (Chote et al. 2021) similar to the transitional feature in EQ Lyn (Mukadam et al. 2013) and in V455 And (Araujo-Betancor et al. 2005). Since in *TESS* only the harmonic is detected, the fundamental is here inferred. This is similar behaviour to that of WZ Sge, where the subsequent harmonics are much stronger than the fundamental signal as is visible in Fig. 1. A parallel may be drawn with the sub-harmonics of QPOs observed in XRBs, where the fundamental signal is the strongest, not the lowest frequency (Casella, Belloni & Stella 2005). The overall unusual behaviour of these signals suggests the necessity of an alternative explanation.

QPOs in XRBs display strikingly similar properties. They show harmonics and time variability as well as general broadness of the signal itself (Ingram & Motta 2019). This is apparent in the quality

factor of the QPOs, which – depending on the type of XRB QPO – can be $Q \lesssim 3$ or $Q \gtrsim 6$. Due to the value of Q depending also on the variability of the signal during the observations, it may be expected that Q will be much larger for AWDs due to the slower variability time-scales. This is indeed the case as shown by the reported Q values in Table 2, where some QPOs have $Q \gtrsim 10000$. This, whereas unusual for XRBs, would seem necessary for a signal to be detected above the Poisson noise-dominated systems such as the ones shown here. However, despite such a high Q value the signals bear little similarity to other coherent signals such as the orbital period as described above and shown in Fig. B1.

5.2 Magnetically driven precession as QPO-driving mechanism

QPOs in XRBs are generally explained by the relativistic effect of frame dragging modelled most commonly by Lense–Thirring precession (Stella & Vietri 1998; Stella, Vietri & Morsink 1999; Psaltis & Norman 2000; Fragile, Mathews & Wilson 2001; Ingram, Done & Fragile 2009). While several possibilities have been presented, in particular for NS XRBs, Lense–Thirring precession is currently the most popular interpretation. However, since AWDs are indisputably non-relativistic, a different model is required to explain their QPOs. A model explored by Warner & Woudt (2002) proposes that a magnetospherically truncated accretion disc may give rise to QPOs from the interaction between twisted magnetic field lines and plasma in the disc. This may produce a dense and elevated region referred to as a 'blob'. The release of energy from the sudden reconnection of strained field lines within the blob is speculated to generate disturbances that propagate through the disc, potentially resonating with its natural oscillations and generating QPOs. In this scenario the frequency of the QPOs are associated with the recconection time-scale estimated in Warner & Woudt (2002) to be of the order of ~15 min for a non-resonant signal. The authors do not consider a resonant case as this would be too close to the orbital period and difficult to detect photometrically. The resulting frequency range thus corresponds to the QPOs and DNOs found by Warner et al. (2003), not the ones reported in this work which occur on longer time-scales.

One alternative and intrinsically non-relativistic model for QPOs in NSs was proposed by Aly & Kuijpers (1990), where the QPOs are driven by interactions between the disc and accretor magnetic field. However, under such framework, the QPOs can only occur at a radius where the magnetic fields strengths of the accretor and disc are equal (equation 2 in Aly & Kuijpers 1990), which may not be a feasible scenario for AWDs.

A further alternative model developed to explain QPOs in NSs and T Tauri stars was developed by Lai (1999). They suggest that QPOs may be associated with magnetically driven precession, a phenomenon where the orientation of the accretion disc surrounding a rotating magnetized star undergoes a periodic wobbling motion around the star's spin axis. This interaction between the disc and the star's rotating magnetic field induces a warping effect on the disc, causing it to deviate from its original equatorial configuration and to precess around the star. The precession torque arises from the interaction between the surface current on the disc and the horizontal magnetic field produced by the star's dipole. The non-linear evolution of the disc's state is then further explored by Pfeiffer & Lai (2004), and the model's applications to NS low-frequency QPOs are discussed in Shirakawa & Lai (2002a, b).

A schematic sketch of the model geometry is shown in Fig. 5. In the framework of this model, as presented by Lai (1999), the star's
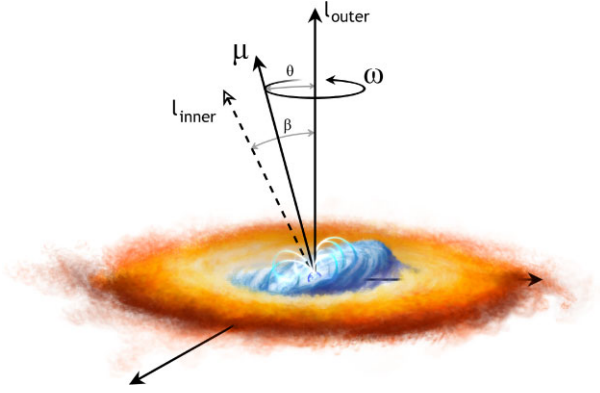
Figure 5. Diagram showing the disc geometry producing a QPO as described by Lai (1999) and Pfeiffer & Lai (2004). The accretor magnetic field vector μ and spin axis ω are misaligned to the angular momentum of the outer standard accretion disc (L_{outer}) leading to the precession of an inner part of the disc that is warped as a consequence (L_{inner}).

rotational axis ω is tilted with respect to the disc's angular momentum (l) by an angle β.

The QPO is generated by the precession of the inner disc around the spin axis of the accretor. Lai (1999) approximates the precession frequency of the entire inner disc by multiplying the magnetic precession frequency of a ring at any specific characteristic radius r, $\nu_p(r)$, by a dimensionless constant A, such that the resulting QPO frequency can be expressed as

$$\nu_{\text{QPO}} = A\nu_p(r) = \frac{A}{2\pi^3} \frac{\mu^2}{r^7 \, \Omega(r) \, \Sigma(r)} \frac{F(\theta)}{D(r)}, \tag{4}$$

where μ is the stellar magnetic dipole moment ($\mu = BR^3$, where B is the field strength and R is the stellar radius of the accretor), Ω is the Keplerian angular frequency, Σ is the disc surface density, and $F(\theta)$ and $D(r)$ are dimensionless functions defined in Appendix C (where we discuss the model in more detail). Because of several degenerate parameters in this model, we here assume that the characteristic radius r is the disc inner radius r_{in} which we set equal to both the magnetospheric radius and the coronation radius such that $r = r_{\text{in}} = r_m = r_{\text{co}}$. A more detailed description of the model and its parameters is given in the Appendix C.

5.2.1 Magnetic field strength, accretion rate, and spin estimation from QPOs in AWDs

Equation (4) depends on several free parameters. Amongst those are the accretor mass and size, the strength of the intrinsic magnetic field strength of the accretor B, the accretion rate of the system $\dot{M}$ and the dimensionless viscosity of the disc α. A different combination of these parameters can yield different QPO frequencies which may occur at different radii. The radius of the QPO is given by the relation between the magnetospheric radius r_M and the corotation radius r_{CO}. We here assume that $r_{\text{in}} = r_M = r_{\text{CO}}$, which allows to break some of the degeneracies in the model when inferring the accretor magnetic field and corresponding spin of the accretor.

To explore the validity of the model, we employ a set of fiducial parameters as several of these would otherwise remain unconstrained. The effect of varying the B field and accretion rate is non-negligible, and no reasonable estimate can be made that would be applicable for all AWDs or NS XRBs. Therefore, we instead explore a range of these parameters for AWDs and NS XRBs as noted in Table 4. Hence, for a given magnetic field and accretion rate a specific combination of

Table 4. Fiducial model parameters for the magnetically driven precession model for QPOs for AWDs and NS XRBs. For the main parameters that are varied through the model, the magnetic field of the accretor B and the accretion rate $\dot{M}$, the ranges are cited instead. For AWDs, 2 values of viscosity and η are given to represent WZ Sge and GW Lib like objects.

Model parameter	AWDs	NS XRBs
M ($M_\odot$)	0.8	1.4
R	$0.01 R_\odot$	10 km
B (G)	$10^3 – 10^8$	$10^7 – 10^{10}$
$\dot{M}$ ($M_\odot$ yr^{-1})	$10^{-12} – 10^{-7}$	$10^{-12} – 10^{-7}$
α	0.006 (WZ Sge), 0.003 (GW Lib)	0.006
η	0.1 (WZ Sge), 0.05 (GW Lib)	0.1
θ ($^\circ$)	45	45
A	0.6	0.6

QPO frequency and spin period is obtained allowing for comparison to data for objects with QPO and spin period measurements.

Specifically, for the purpose of comparing the model to the two observed QPOs in AWDs with spin period measurements, two separate values of viscosity are chosen. These correspond to the quiescent values of WZ Sge with $\alpha \sim 0.006$ and 0.003 (Howell, Szkody & Cannizzo 1995) for GW Lib, which are obtained from modelling of the recurrence time-scales of the dwarf novae outbursts. For other objects, the viscosity of WZ Sge as well as other values of fiducial parameters are used. The different fiducial parameters are due to the intrinsic differences between the systems. Despite both being dwarf novae with similar characteristics and recurrence times of the outbursts ($\sim$ years), the estimates of their viscosities from Howell et al. (1995) provide an important constraint on otherwise fully unconstrained fiducial parameters. Ideally, to truly apply the magnetically driven QPO model to its full extent a precise measurement of all parameters is required. With this not feasible, it is necessary to use these viscosity estimates. Since the estimated accretion rate of GW Lib from the literature (Hilton et al. 2007) is much smaller than that of WZ Sge, the fiducial parameters of GW Lib are used in the treatment of the other objects showing QPO.

For the fiducial values of these parameters and each combination of B and $\dot{M}$, there is a characteristic QPO frequency $\nu_{\rm QPO}$ with an associated spin period $P_{\rm spin}$. A variation in the assumption of $r_{\rm in} = r_{\rm M} = r_{\rm CO}$ would therefore result in variation of $P_{\rm spin}$ and $\nu_{\rm QPO}$ pairs for corresponding B and $\dot{M}$ pairs.

Fig. 6 demonstrates the dependence of the model on these four parameters. In the right-hand side panels, the QPO frequency is plotted as a function of $P_{\rm spin}$. The dashed lines then show lines of equal B and the solid lines the lines of equal $\dot{M}$. A QPO measurement can in such a case be used to put constraints on B and and accretion rate for a given spin. Since there is a strong correlation between the B and accretion rate in the model, the same plots are also shown in the left-hand side panels where $P_{\rm spin}$ is scaled by the magnetic field strength and the accretion rate.

By evaluating the magnetically driven precession model for the fiducial model values and the B and $\dot{M}$ ranges listed in Table 4 it is possible to estimate these parameters and the corresponding spin period of the accretor. The WD mass is fixed to $0.8 M_{\rm WD}$ for all objects as a good approximation for the mean of the AWD accretor mass distribution (Zorotovic, Schreiber & Gänsicke 2011; Pala et al. (2022). The WD radius is then derived from Hamada & Salpeter (1961); Nauenberg (1972) using the WD mass. η, the parameter relating Alfvén and magnetospheric radius, is set to 0.1 and 0.05.

For strongly magnetic systems such as NS and magnetic AWDs, it is by convention set to 0.5 (Ghosh & Lamb 1979; Mönkkönen et al. 2022). However, the model requires the magnetospheric radius to be equal to the co-rotation radius. This is not likely to always be the case and a smaller value of η required here may reflect that. θ is set to the midpoint value of 45°. A is fixed to 0.6 as this is the average of the range determined for the parameter in the framework of this model in Shirakawa & Lai (2002a).

To compare how successfully the model predicts B, $\dot{M}$, and spin for a particular QPO frequency, it is possible to use the cases of WZ Sge and GW Lib. To estimate B and $\dot{M}$ from the model a fine grid of B and $\dot{M}$ is computed with a pair of spin and QPO frequency corresponding to each pair of B and $\dot{M}$. Then for a given measurement of spin and QPO frequency with their corresponding uncertainties the corresponding range of B and $\dot{M}$ can be extracted.

WZ Sge has an estimated spin period of 27.87 ± 0.01 s as measured by Patterson (1980). Later in Patterson et al. (1998) the magnetic field is invoked to be between 1 and 5×10^4 G. This is necessary to explain the disappearance of the potential spin frequency during an outburst when the accretion rate of a dwarf nova such as WZ Sge rises by a factor of ~ 1000 from the quiescent rate of $\sim 1 \times 10^{-11} M_\odot$ yr^{-1}. With this information it is possible to compare the observables of WZ Sge to the parameter space in the top panel of Fig. 6. The QPO and spin frequency with the assumed B range and $\dot{M}$ correspond to the correct range within the parameter space, showing that the model can reproduce reasonable results for the fiducial values of fixed parameters, with B $= 2.5 \pm 0.1 \times 10^4$ G and $\dot{M} = 4.0 \pm 0.3 \times 10^{-13} M_\odot$ yr^{-1}. This value is at odds with the previously reported quiescent accretion rate for WZ Sge. An important point to consider is that in the model the accretion rate represents the accretion rate on to the accretor, not the mass transfer rate from the donor. Furthermore, because there are a set number of fixed fiducial parameters, an error estimate on the model's parameter prediction is only meaningful when considering the potential variability of the free parameters that remain fixed. Hence, the errors here only represent a snapshot of the real uncertainty contours and so should be treated as a lower limit on the real errors.

Similarly for GW Lib, the spin period was measured to be 209 s from the UV line widths (Szkody et al. 2012). As the recurrence time-scale for GW Lib is very long ($\sim$ years) the quiescent viscosity is also low (Howell et al. 1995). Adapting the fiducial model parameters from Table 4 the resulting B field and accretion rate estimate are B $= 2.0 \pm 0.1 \times 10^5$ G and $\dot{M} = 2.2 \pm 0.3 \times 10^{-14} M_\odot$ yr^{-1}. This leads to a higher magnetic field compared to WZ Sge and extremely low accretion rate. Nevertheless, such a low accretion rate has been reported for quiescent state of GW Lib by Hilton et al. (2007). However, given the lack of constraint on some of the model parameters, this should be treated more as a rough estimate. The parameter space for GW Lib and its adapted fiducial parameters are shown in the bottom panel of Fig. 6.

As there are no estimates for spin period, B or $\dot{M}$ for any of the other systems, only very broad ranges can be provided for the model parameters, adopting $\alpha = 0.006$ and $\eta = 0.1$. The only exception is V3101 Cyg, which has theoretically predicted $\alpha < 0.005$ (Hameury & Lasota 2021) and so the fiducial parameters of GW Lib are used instead. In such a case it is impossible to provide reasonable constraint on any of the parameters. However, previously reported values of accretion rate can help constrain the estimates of B field and spin. The accretion rates used are $1 – 2 \times 10^{-10} M_\odot$ yr^{-1} from Veresvarska et al. (2024) for CP Pup, $\sim 10^{-7} – 10^{-6} M_\odot$ yr^{-1} for T Pyx from Godon et al. (2018) and $\sim 10^{-11} – 10^{-10} M_\odot$ yr^{-1} for V3101 Cyg which is a WZ Sge type Dwarf Nova. The corresponding B and
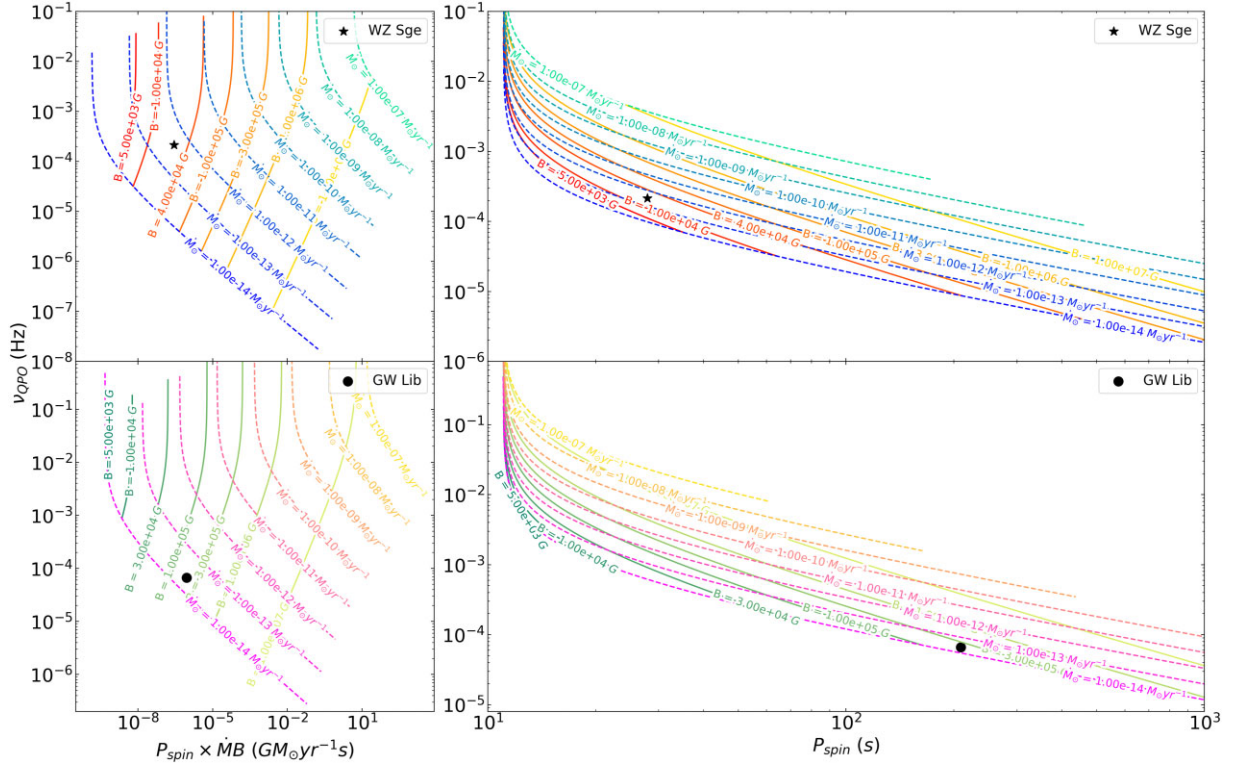
Figure 6. Right panel: model QPO frequency as a function of the corresponding accretor spin. Left panel: model QPO frequency as a function of the corresponding accretor spin scaled by the accretion rate and magnetic field strength of the accretor. In all panels, the dashed lines denote lines of equal *B* field and solid lines denote lines of equal accretion rate. Top panels: fiducial parameters corresponding to WZ Sge from Table 4. The star corresponds to the observed QPO and spin, scaled by *B* and accretion rate on the right. Bottom panels: same as top panels but with fiducial parameters of GW Lib from Table 4. The filled circle represents the observed QPO and scaled spin of GW Lib.

Table 5. Estimates of magnetic field strength, accretion rate, and spin period from the magnetically driven precession model of QPO in AWDs. The values should be treated as possible ranges and not as best-fitting values. In the case of WZ Sge and GW Lib, the parameters can be constrained better using the observational estimates of $P_{\rm spin}$, which are noted in the table instead and denoted by $*$. For objects with unknown spin, an estimate of accretion rate is used so that [a]Veresvarska et al. (2024), [b]Godon et al. (2018) and [c]$\sim 10^{-11}-10^{-10}\,{\rm M}_\odot\,{\rm yr}^{-1}$ as a representative value for the WZ Sge-type Dwarf Nova V3101 Cyg. CP Pup and T Pyx use the fiducial parameters of WZ Sge and V3101 Cyg of GW Lib.

Object	B (G)	$\dot{M}({\rm M}_\odot\,{\rm yr}^{-1})$	$P_{\rm spin}$ (s)
CP Pup	$2-3 \times 10^5$	$1-2 \times 10^{-10\,a}$	$72-84$
WZ Sge	$2.5^{+0.1}_{-0.1} \times 10^4$	$4.0^{+0.3}_{-0.3} \times 10^{-13}$	$27.87^{+0.01}_{-0.01}*$
GW Lib	$1.97^{+0.14}_{-0.12} \times 10^5$	$2.2^{+0.3}_{-0.3} \times 10^{-14}$	$209*$
T Pyx	$9 \times 10^6 - 1 \times 10^7$	$10^{-7}-10^{-6\,b}$	$148-345$
V3101 Cyg	$3 \times 10^3 - 1.2 \times 10^4$	$10^{-11}-10^{-10\,c}$	$99-165$

spins are listed in Table 5, alongside the accretion rate estimates for WZ Sge and GW Lib. The obtained *B* field is below the standard values of confirmed magnetic systems, apart from T Pyx, and all estimated spin ranges are under 3 min, apart from T Pyx, where the range of possible spins reaches ∼6 min.

It is, however, necessary to note that all such deductions on the magnetic field strength and accretion rate are highly dependent on a good understanding of the system. As of now, there are no known systems in which there is sufficient certainty to constrain the values of the fiducial parameters. As a consequence all deduced constraints

on *B* and $\dot{M}$ are simply a reflection of the constraints on the spin and QPO frequency measurements. Hence, the results reported in Table 5 should be treated with extreme caution and mostly serve as a prediction of the potential precision, subject to future precise measurements of parameters in Table 4.

5.2.2 QPO model implications for spin, B field, and accretion rate measurement

Fig. 6 shows that for the current set up of the model, all AWDs showing QPOs with similar characteristics as WZ Sge would be expected to have a relatively fast spin ∼20–200 s WD. This is assuming a low magnetic field $B \lesssim 10^6$ G and low accretion rate $< 10^{-10}{\rm M}_\odot\,{\rm yr}^{-1}$ and a similar frequency range for the QPOs as observed in the systems here. The extremely low accretion rates recovered by the model here should be taken as representative of the instantaneous accretion rate on to the accretor, not the mass transfer rate from the donor star. Hence, such low values may not be unrealistic for the accumulation of mass between Dwarf Novae outbursts in WZ Sge and GW Lib, in particular, in the case of GW Lib (Hilton et al. 2007).

For slowly spinning systems $\gtrsim 1000$ s, the QPOs in weakly magnetized systems adopting parameters self-similar to the fiducial ones used here would yield QPO frequencies $\lesssim 10^{-6}$ Hz (278 h). This would provide a considerable observational challenge with the current data. New potential missions such as *PLATO* may help uncover these in the future. For magnetic systems, monitoring of close-by and bright magnetic systems, such as the intermediate

polars V1223 Sgr or FO Aqr, may unveil new QPOs in systems with alternative values of *B* and direct spin observations to use for model verification. These potential detections could then be used to put a better constraint on some of the fiducial parameters in Table 4.

Given that the QPOs reported here are mostly observed in either dwarf novae or nova-likes the potential variability of the QPO with a large change of accretion rate could also provide important insight on the nature of the QPOs themselves and the systems in which they occur as well as their driving mechanism.

5.3 Break and QPO correlation in XRBs and AWDs and QPO driving mechanism implications

Type-C and HBO QPOs in XRBs bear several observational similarities to the QPOs reported here in AWDs. An important characteristic of these QPOs in XRBs is their correlation to a low-frequency break (Wijnands & van der Klis 1999). The QPOs in AWDs reported here appear to follow the same correlation. Type-C and HBO QPOs in XRBs are usually explained by the relativistic effect of frame dragging. In such a case, it can be assumed that the PSD break is associated to the viscous frequency at the inner-edge of the precessing flow (Ingram et al. 2009; Ingram & Done 2011).

This cannot be the case in the non-relativistic AWDs. However, in the framework of the magnetically driven precession model as described in Section 5.2 the observational characteristics of the QPOs are similar, despite a different driver behind the behaviour. A precessing inner flow of the accretion disc would also in this case be expected to produce a PSD break at the viscous frequency associated to the corresponding radius. This would have the effect of producing a break at a lower frequency than the QPO and a relation between the two quantities, as observed in Fig. 7.

In Fig. 7, we reproduce the data from Fig. 4, but now overplay several models. As in Fig. 4, the black circles represent the BH QPOs and their breaks from Wijnands & van der Klis (1999), the red squares represent the NS QPOs and their corresponding breaks from Wijnands & van der Klis (1999). The cyan diamonds represent the AWD QPOs and breaks from Table 2. The shaded regions represent the model parameter spaces for Lense–Thirring precession for BH XRBs, magnetically driven precession for NS XRBs and AWDs. The cyan-shaded regions overlapping with the observed AWD QPOs represents the parameter space in which QPOs in AWDs can be explained by magnetically driven precession for all parameters shown in Table 4. The viscous frequency, ν_{visc}, was obtained from the dynamical frequency, ν_{dyn} at the QPO radius such that $\nu_{\mathrm{visc}} = \alpha (\frac{H}{R})^2 \nu_{dyn}$, and by assuming a value for $\alpha \left(\frac{H}{R}\right)^2 \sim 5 \times 10^{-5}$. $\alpha \left(\frac{H}{R}\right)^2$ is treated here as a standalone parameter, not a combination of viscosity α and the scale height ratio $\frac{H}{R}$. This is because in the context of AWDs there have been measurements of $\alpha \left(\frac{H}{R}\right)^2$ parameters that can be used to estimate this parameter (Scaringi 2014; Veresvarska & Scaringi 2023). Whereas estimates of α have been measured (Howell et al. 1995; Kotko & Lasota 2012), no tangible constraint is known for $\frac{H}{R}$. Therefore, treating $\alpha \left(\frac{H}{R}\right)^2$ as a single parameter based on previous measurements is deemed as the more appropriate assumption. The value is chosen as the middle of the expected range for this parameter for AWDs in quiescence. The potential range is considered for α to be between 10^{-3} for long recurrence dwarf novae such as GW Lib (Howell et al. 1995) up to 10^{-1} for high-accretion-rate systems (Kotko & Lasota 2012), such as T Pyx. The estimated range for $\alpha \left(\frac{H}{R}\right)^2 \sim 1 \times 10^{-7}$–$1 \times 10^{-3}$. The implications of the uniform assumption of $\alpha \left(\frac{H}{R}\right)^2 \sim 5 \times 10^{-5}$

with the range of $\alpha \sim 1 \times 10^{-3}$–0.1 (Howell et al. 1995; Kotko & Lasota 2012) is that the $\frac{H}{R} \sim 0.2$–0.02.

The *x*-axis of Fig. 7 is the viscous frequency at the QPO radius. This demonstrates that all the QPOs reported here could be explained by the magnetically driven precession model, bearing in mind the upper limit on the break frequencies in all objects apart from WZ Sge. Therefore, a potential test of this model and correlation would be the measurement of break frequencies for these systems and whether it deviates from the current limit by more than an order of magnitude. Such a test would, however, require more data, either an extension of the existing *TESS* time series or a new long-term mission such as *PLATO*.

The red-shaded region overlapping with observed QPOs in XRBs and ranging from $\sim 10^{-4}$ to 10^0 Hz for the viscous frequency corresponds to the parameter space where the NS XRB QPOs and their PSD breaks can be explained by the magnetically driven precession. The parameter space was constructed for an NS with $M_{\mathrm{NS}} \sim 2\,\mathrm{M}_\odot$, $R_{\mathrm{NS}} \sim 10$ km, $B \sim 10^7$–10^{10} G, the same accretion rate range, θ and A as in Table 4. η was fixed to 0.1 and α to 0.006 for consistency with the AWDs. $\alpha \left(\frac{H}{R}\right)^2$ was assumed the same as in AWDs.

The black-shaded region overlapping with QPOs in XRBs from $\sim 10^{-1}$ to 10^2 Hz corresponds to the parameter space where the QPOs in XRBs can be explained by Lense–Thirring precession. QPOs driven by Lense–Thirring precession occur at a characteristic frequency which is related to the precession of a solid disc as detailed in Ingram et al. (2009):

$$\nu_{\mathrm{LT}} = \frac{(5 - 2\zeta)}{\pi(1 + 2\zeta)} \frac{a \left(1 - \left(\frac{r_i}{r_o}\right)^{\frac{1}{2}+\zeta}\right)}{r_o^{\frac{5}{2}-\zeta} r_i^{\frac{1}{2}+\zeta} \left[1 - \left(\frac{r_i}{r_o}\right)^{\frac{5}{2}-\zeta}\right]} \frac{c}{R_g}, \tag{5}$$

where a is the BH spin, c is the speed of light in vacuum, r_i the inner radius of the precessing flow in the units of R_g, and r_o the outer radius of the precessing flow in the units of R_g. R_g represents the gravitational radius $R_g = \frac{GM}{c^2}$. ζ is the index governing the radial dependence of surface density and is here fixed to 0 as from simulations as in Ingram et al. (2009). The mass range accounted for in the parameter space spans BH mass from 3 to 20 $\mathrm{M}_\odot$ and spins from 0 to 0.998. The outer radius of the precessing region is considered between 1.01 and 50 R_g and associated to r_o. The inner radius is here fixed to the innermost stable circular orbit (ISCO) based on the spin. This can predict larger QPO frequencies in BHs than are observed and the upper limit of the parameter space should be treated with caution. This is usually accounted for by setting the inner disc radius to the bending wave radius (Ingram et al. 2009) which would require the assumption of $\frac{h}{r}$ ratio. As this is unknown and could introduce another free parameter, the inner disc radius is here fixed at ISCO for simplicity. The viscous frequency is determined for radius r_o with $\alpha \left(\frac{H}{R}\right)^2 \sim 10^{-3}$ as is usually assumed for BH XRBs (Ingram et al. 2009).

For all the parameter spaces detailed above for Lense–Thirring precession and magnetically driven precession, it is clear that that both follow the same observational trend behind the QPO and break relation, irrespective of the driver mechanism of the QPO. This unfortunately also means that the relation cannot be used to disentangle the nature of the driving mechanism for QPOs in XRBs since the two parameter spaces overlap. However, the non-relativistic AWDs show tentatively, whilst bearing in mind the uncertainty from the upper limits on most breaks in AWDs, that magnetically
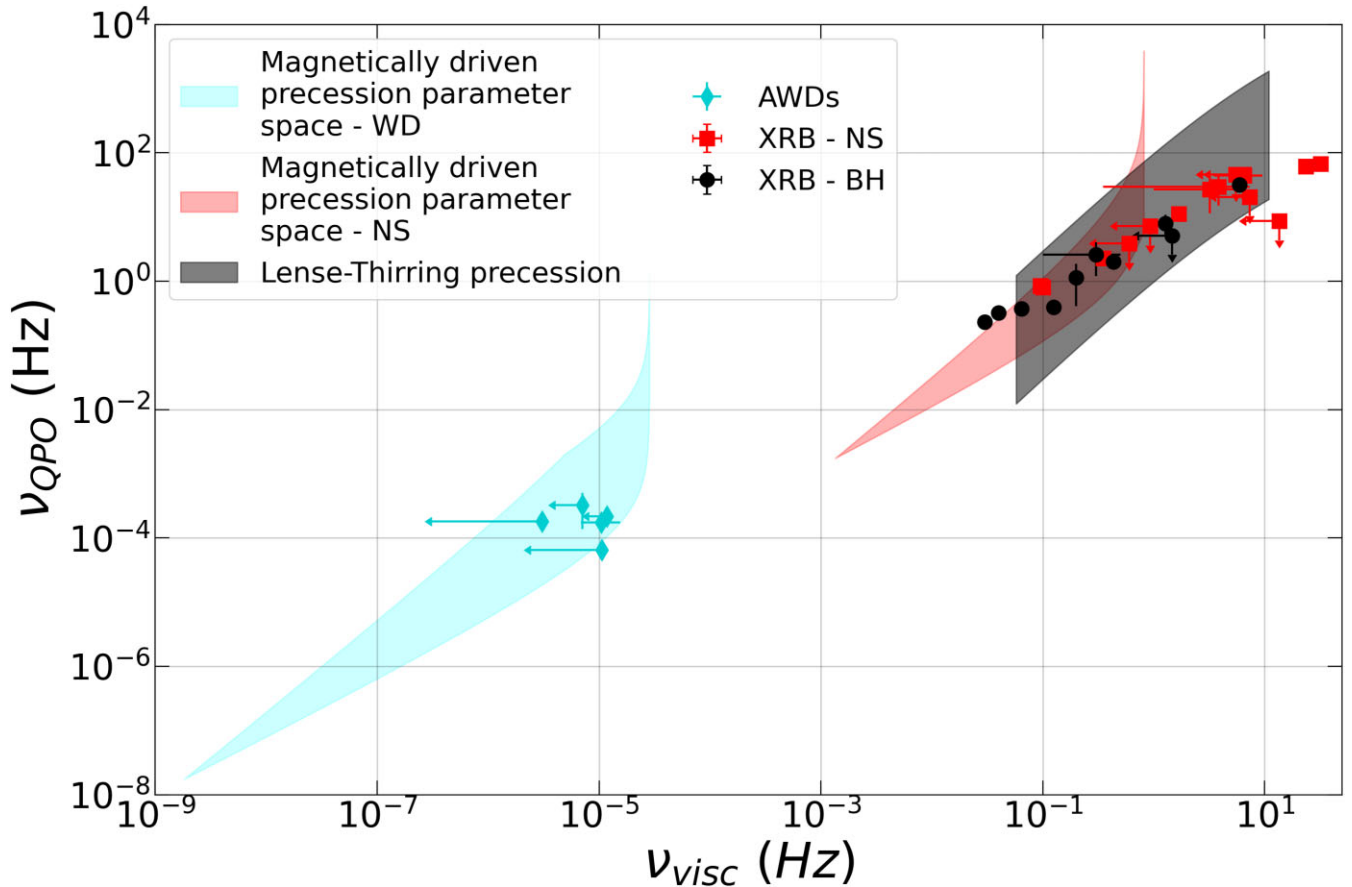
Figure 7. QPO frequency as a function of the viscous frequency at the QPO radius. The shaded regions correspond to the predicted model parameter space of QPOs and their viscous frequency. The lowest shaded region between $\nu_{\mathrm{visc}} \sim 10^{-10}$ and 10^{-4} Hz represents the model parameter space of AWD QPOs as predicted by magnetically driven precession. For NS XRBs the magnetically driven precession model predicts a parameter space shown by the shaded region between $\nu_{\mathrm{visc}} \sim 10^{-4}$ and 10^0 Hz. The partially overlapping shaded region between $\nu_{\mathrm{visc}} \sim 10^{-1}$ and 10^2 Hz represents the parameter space of QPOs in BH XRBs as predicted by Lense–Thirring precession. The observed QPOs with their corresponding low-frequency breaks (ν_{visc} are denoted for AWDs in diamonds, for NS XRBs in squares and in filled circles for BH XRBs.).

driven precession is a viable method for inducing QPOs in weakly magnetized AWDs.

6 CONCLUSIONS

QPOs are a well-known characteristic in both XRBs and AWDs. In XRBs, they are well-defined phenomena with different types according to their observational characteristics and correlation with broad-band structure. However, in AWDs, QPOs usually refer to unexplained, transitional and somewhat coherent signals observed in the light curves. Here, we report five persistent QPOs in low magnetic field AWDs showing similar properties to type-C QPOs in XRBs, such as harmonics. A tentative link to the QPOs in XRBs is that the QPOs in AWDs seem to follow the correlation of XRB QPOs with a broad-band low-frequency break, when assuming that the upper limits on the break frequencies are representative of their true value. The break is usually associated with the viscous frequency of the outer part of the precessing flow of the disc where the QPOs are generated. Furthermore, the reported QPOs in AWDs show a low-frequency broad-band structure, which can be fitted with a zero-centred Lorentzian as in XRBs or with a power law, at a frequency where such a flow transition would be expected.

Due to the non-relativistic nature of AWD systems, we propose that the QPOs are driven by a weak magnetic field of the accretor being misaligned to the disc normal and causing precession of the inner part of the accretion disc. This model was previously considered for being part of the driving mechanism behind the low-frequency QPOs in NS XRBs and potentially T Tauri stars. Here, we show an implementation for AWDs, whose magnetic fields lie in between those of NS and T Tauri stars.

WZ Sge shows a QPO at $\sim 2 \times 10^{-4}$ Hz ($\sim$77 min) and GW Lib at $\sim 7 \times 10^{-5}$ Hz ($\sim$4.3 h), with both exhibiting harmonics. They are also the only systems in the sample with spin period measurements. We report that the model prediction for a QPO at these frequencies requires accretion rate and spin that are consistent with the observationally reported values. This could present a possibility for magnetic field and spin estimates in weakly magnetic AWDs where direct measurements of these quantities are not yet possible. As an example, we give estimates for these parameters for the rest of our sample. However, such predictions, together with the corresponding uncertainties, can only be obtained within the framework of the inherent assumptions of the model, once reasonable estimates on the fiducial parameters can be obtained. Therefore, the results here can only serve as an illustration of the potential capabilities of the

model, until a more detailed measurement of the fiducial parameters is obtained with the help of future missions such as *PLATO*.

DATA AVAILABILITY

The *TESS* data used in the analysis of this work is available on the MAST webpage https://mast.stsci.edu/portal/Mashup/Clients/Mast/Portal.html. The *ASAS-SN* data (Shappee et al. 2014; Kochanek et al. 2017) used for the calibration of *TESS* data is available on the *ASAS-SN* webpage https://asas-sn.osu.edu/.

REFERENCES

Aly J. J., Kuijpers J., 1990, A&A, 227, 473
Araujo-Betancor S. et al., 2005, A&A, 430, 629
Belloni T. M., Motta S. E., 2016, in Bambi C., ed., Astrophysics and Space Science Library Vol. 440, Astrophysics of Black Holes: From Fundamental Aspects to Latest Developments. Springer-Verlag, Berlin, p. 61
Belloni T., Psaltis D., van der Klis M., 2002, ApJ, 572, 392
Bruch A., 2022, MNRAS, 514, 4718
Casella P., Belloni T., Stella L., 2005, ApJ, 629, 403
Chote P. et al., 2021, MNRAS, 502, 581
Cropper M., 1990, Space Sci. Rev., 54, 195
Fragile P. C., Mathews G. J., Wilson J. R., 2001, ApJ, 553, 955
Frank J., King A., Raine D., 2002, Accretion Power in Astrophysics, 3rd edn. Cambridge Univ. Press, Cambridge
Ghosh P., Lamb F. K., 1979, ApJ, 234, 296
Godon P., Sion E. M., Williams R. E., Starrfield S., 2018, ApJ, 862, 89
Groot P., Bloemen S., Vreeswijk P. e. a., 2024, preprint(arXiv:2405.18923v2)
Hamada T., Salpeter E. E., 1961, ApJ, 134, 683
Hameury J. M., Lasota J. P., 2021, A&A, 650, A114
Hilton E. J., Szkody P., Mukadam A., Mukai K., Hellier C., van Zyl L., Homer L., 2007, AJ, 134, 1503
Homan J., 2001, PhD thesis, Univ. Amsterdam, Netherlands
Howell S. B., Szkody P., Cannizzo J. K., 1995, ApJ, 439, 337
Ingram A., Done C., 2011, MNRAS, 415, 2323
Ingram A. R., Motta S. E., 2019, New Astron. Rev., 85, 101524
Ingram A., Done C., Fragile P. C., 2009, MNRAS, 397, L101
Kochanek C. S. et al., 2017, PASP, 129, 104502

Kotko I., Lasota J. P., 2012, A&A, 545, 1
Kupfer T. et al., 2015, MNRAS, 453, 483
Lai D., 1999, ApJ, 524, 1030
Littlefield C., Scaringi S., Garnavich P., Szkody P., Kennedy M. R., Iłkiewicz K., Mason P. A., 2021, AJ, 162, 49
Lomb N. R., 1976, Ap&SS, 39, 447
Lubow S. H., 1991, ApJ, 381, 259
Mönkkönen J., Tsygankov S. S., Mushtukov A. A., Doroshenko V., Suleimanov V. F., Poutanen J., 2022, MNRAS, 515, 571
Mukadam A. S. et al., 2013, AJ, 146, 54
Nauenberg M., 1972, ApJ, 175, 417
Norton A. J., Wynn G. A., Somerscales R. V., 2004, ApJ, 614, 349
Norton A. J., Butters O. W., Parker T. L., Wynn G. A., 2008, ApJ, 672, 524
Pala A. F. et al., 2022, MNRAS, 510, 6110
Patterson J., 1980, ApJ, 241, 235
Patterson J., Robinson E. L., Nather R. E., 1977, ApJ, 214, 144
Patterson J., Richman H., Kemp J., Mukai K., 1998, PASP, 110, 403
Pfeiffer H. P., Lai D., 2004, ApJ, 604, 766
Psaltis D., Norman C., 2000, preprint(astro-ph/0001391)
Scargle J. D., 1998, ApJ, 504, 405
Scaringi S., 2014, MNRAS, 438, 1233
Scaringi S., Körding E., Uttley P., Groot P. J., Knigge C., Still M., Jonker P., 2012, MNRAS, 427, 3396
Scaringi S. et al., 2022, Nature, 604, 447
Shappee B. J. et al., 2014, ApJ, 788, 1
Shirakawa A., Lai D., 2002a, ApJ, 564, 361
Shirakawa A., Lai D., 2002b, ApJ, 565, 1134
Solanki S., Kupfer T., Blaes O., Breedt E., Scaringi S., 2021, MNRAS, 500, 1222
Solheim J.-E. S. E., 2010, PASP, 122, 1133
Stella L., Vietri M., 1998, ApJ, 492, L59
Stella L., Vietri M., Morsink S. M., 1999, ApJ, 524, L63
Szkody P. et al., 2012, ApJ, 753, 158
Thorstensen J. R., Patterson J., Kemp J., Vennes S., 2002, PASP, 114, 1108
Timmer J., König M., 1995, A&A, 300, 707
Townsley D. M., Bildsten L., 2004, ApJ, 600, 390
Townsley D. M., Arras P., Bildsten L., 2016, preprint (arXiv:1601.02046)
Veresvarska M., Scaringi S., 2023, MNRAS, 518, 5576
Veresvarska M., Scaringi S., Hagen S., De Martino D., Done C., Ilkiewicz K., Knigge C., Littlefield C., 2024, MNRAS, 529, 664
Warner B., 2004, PASP, 116, 115
Warner B., Robinson E. L., 1972, Nat. Phys. Sci., 239, 2
Warner B., Woudt P. A., 2002, MNRAS, 335, 84
Warner B., van Zyl L., 1998, in Deubner F.-L., Christensen-Dalsgaard J., Kurtz D., eds, New Eyes to See Inside the Sun and Stars, Vol. 185. Springer Dordrecht, p. 321
Warner B., Woudt P. A., Pretorius M. L., 2003, MNRAS, 344, 1193
Wijnands R., van der Klis M., 1999, ApJ, 514, 939
Wood M. A., Thomas D. M., Simpson J. C., 2009, MNRAS, 398, 2110
Woudt P. A., Warner B., Pretorius M. L., Dale D., 2005, in Hameury J. M., Lasota J. P., eds, ASP Conf. Ser. Vol. 330, The Astrophysics of Cataclysmic Variables and Related Objects. Astron. Soc. Pac., San Francisco, p. 325
Zorotovic M., Schreiber M. R., Gänsicke B. T., 2011, A&A, 536, A42

APPENDIX A: *TESS* LIGHT CURVES

Fig. A1 shows the *TESS* light curves of AWDs used in this work apart from CP Pup as noted in Table 1. To demonstrate more clearly the variability on the QPO time-scale a running average of the light curve is overlaid on top of the data in solid black line.
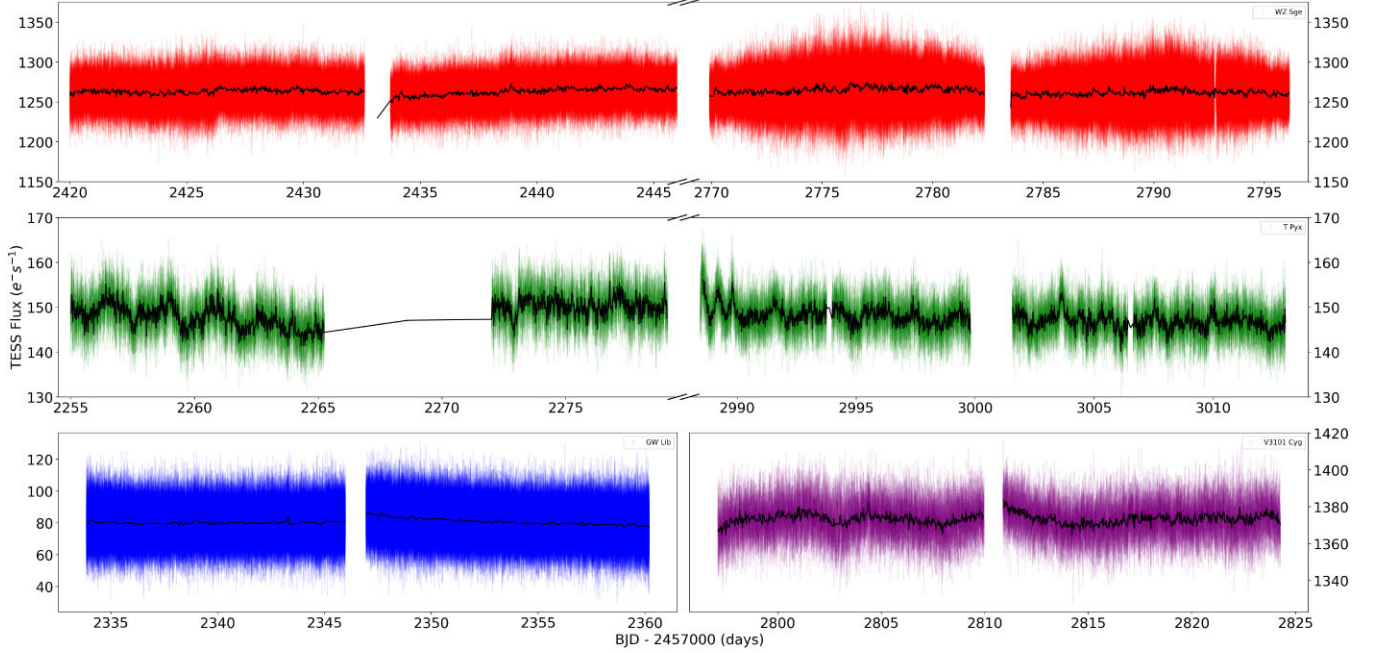
Figure A1. Light curve of WZ Sge, GW Lib, T Pyx, and V3101 Cyg showing all sectors of *TESS* data as described in Table 1 (CP Pup is shown in fig. 1 of Veresvarska & Scaringi 2023). The gap between the individual *TESS* sectors in WZ Sge and GW Lib has been excluded. The solid line in each panel denotes the running average of the light curve on the QPO time-scale.

APPENDIX B: LINEAR PSDS OF QPOS

Fig. B1 shows the linear non-averaged PSD of the light curves from Table 1. The PSDs are zoomed in on the frequency range where the QPOs and their harmonics are the most dominant. In this case, the orbital period signals are not removed to demonstrate the difference between the QPOs and a coherent orbital period. For WZ Sge, the first harmonic of the QPO is not visible due to the first harmonic of the orbit. Other high-frequency harmonics of the QPO and orbit are present but not shown in the frequency range displayed here. For GW Lib only, the first harmonic of the QPO is shown as the fundamental of the signal observed in Chote et al. (2021).
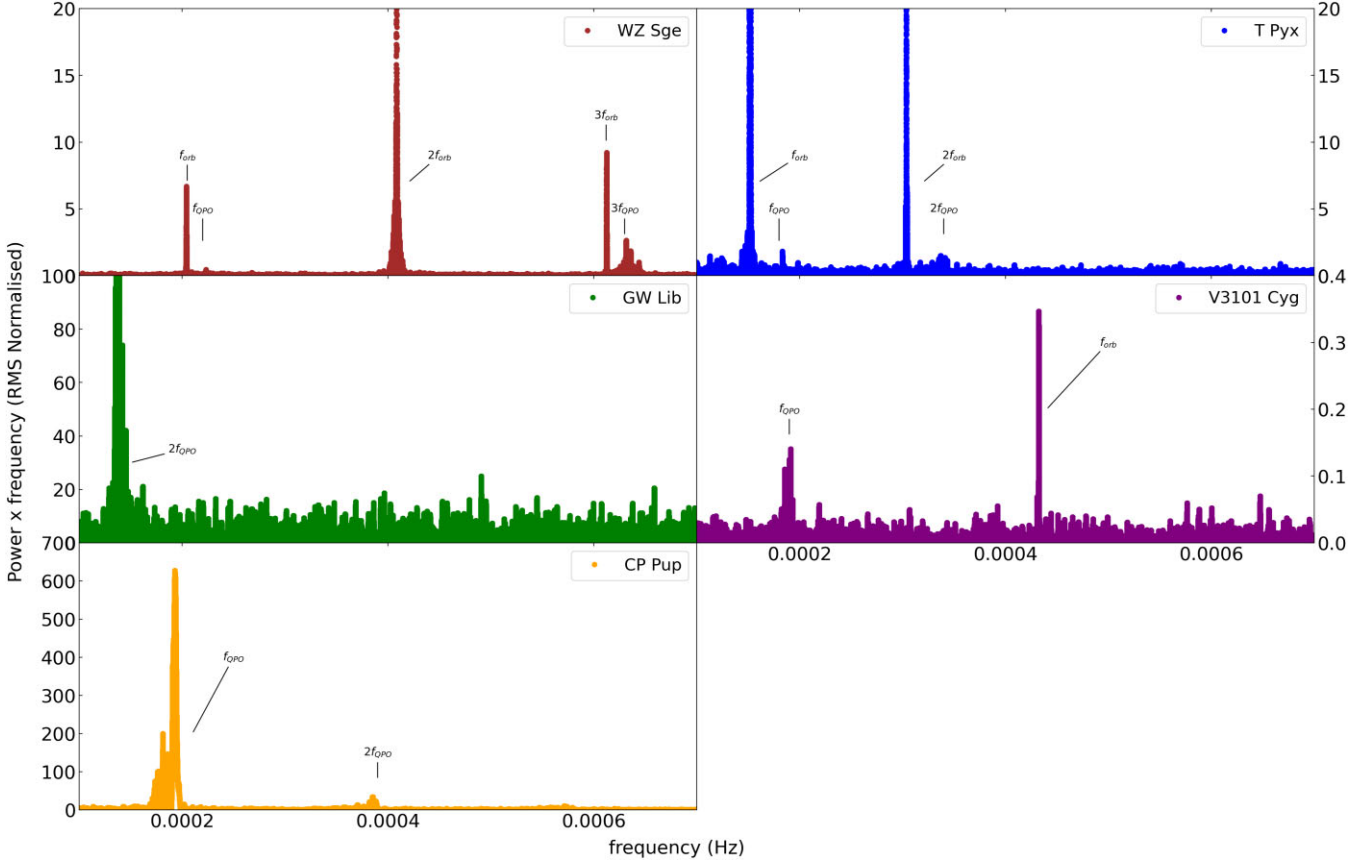
Figure B1. A zoom-in on a section of PSD of light curves from Table 1 with labelled QPO and orbital period signals. The frequency range is fixed to be the same for all panels. Some of WZ Sge harmonics were excluded for better visualization.

APPENDIX C: QPO MODEL: MAGNETICALLY DRIVEN PRECESSION MODEL

The magnetically driven precession model of QPOs discussed in this section was developed by Lai (1999) for the purpose of explaining QPOs in NSs and T Tauri stars. In this frame work, the accretor's spin axis is misaligned to the angular momentum of the accretion disc causing magnetic and warping torques. These torques warp the inner part of the disc which then precesses around.

The magnetospheric radius at which the accretion flow is disrupted by the accretor's magnetic field B is given by

$$r_\mathrm{M} = \eta \left(\frac{2\pi^2}{\mu_0^2} \frac{\mu^4}{GM\dot{M}^2} \right)^{1/7}, \tag{C1}$$

where η is a dimensionless parameter describing the geometry of the accretion flow and the relation between the Alfvén and magnetospheric radius. It is usually set to 0.5 for magnetic systems, but a lower value could indicate that the assumption of $r_\mathrm{M} = r_\mathrm{CO}$, typically assumed for magnetic systems, is not valid (i.e. for a low magnetic field). Such a scenario (low value of η) could also be possible for a system with high inclination. μ is the stellar magnetic dipole moment such that $\mu = BR^3$, M is the accretor mass, R is the accretor radius, $\dot{M}$ is its accretion rate, G is the gravitational constant and μ_0 is the vacuum permeability. Following Lai (1999) and Pfeiffer & Lai (2004), the magnetospheric radius from C1 is set

to be equal to the co-rotation radius:

$$r_\mathrm{CO} = \left(\frac{GMP_\mathrm{spin}^2}{4\pi^2} \right)^{1/3}, \tag{C2}$$

where P_spin is the spin period of the accretor. This assumption of co-rotation radius being equal to magnetospheric radius is a simplification and may not be entirely realistic. This radius is also set to be equal to the inner disc radius r_in. With these assumptions, the global precession frequency of the inner flow is given by

$$\nu_\mathrm{QPO} = A \frac{\Omega_\mathrm{p}(r_\mathrm{in})}{2\pi} = \frac{A}{2\pi} \frac{\mu^2}{\pi^2 r^7 \Omega(r) \Sigma(r) D(r)} F(\theta), \tag{C3}$$

where A is related to the offset between the global precession frequency and the magnetically driven precession frequency. Depending on the details of the disc structure at $r_\mathrm{in} = r_\mathrm{M}$, $A \simeq 0.3-0.85$, as determined by Shirakawa & Lai (2002b). $\Omega(r)$ is the Keplerian frequency at a radius r, $\Sigma(r)$ is the surface density as determined in equation (5.41) in Frank, King & Raine (2002). $D(r)$ is a dimensionless function given by

$$D(r) = \max\left(\sqrt{\frac{r^2}{r_\mathrm{in}^2} - 1}, \sqrt{\frac{2H(r)}{r_\mathrm{in}}} \right), \tag{C4}$$

where $H(r)$ is the half-height of the disc at radius r, as defined in equation (5.41) in Frank et al. (2002). $F(\theta)$ is a function that depends on the dielectric property of the disc, so that $F(\theta) = 2f\cos^2\theta - \sin^2\theta$, where θ is the angle between the magnetic moment of the accretor and the angular momentum of the disc. f is a dimensionless

number between 0 and 1, so that for $f = 1$ all the vertical field is screened out by the disc, whereas for $f = 0$ only the spin-variable vertical field is. We follow Pfeiffer & Lai (2004) in taking $f = 0$ throughout this work for simplicity.

Though the QPO can happen at any radius r the degeneracy this would create would not allow to test the model through observations.

However, assuming $r_{in} = r_M = r_{CO} = r$ mitigates this. Through $r_{in} = r_M = r_{CO}$, the precession and QPO frequency depend on the spin of the accretor, providing a potential handle on the spin period of systems in which it cannot be directly measured, such as weakly magnetic AWDs. Naturally, the model is dependent on many other parameters, chiefly among them the strength of the intrinsic magnetic field strength of the accretor B, the accretion rate of the system $\dot{M}$ and the viscosity of the disc α.

This paper has been typeset from a TeX/LaTeX file prepared by the author.